Characterization of High Speed and Arbitrary Headwall Injection Effects on the Trkalian Swirling Mean Flowfield in Rocket Motors

by

Orie M. Cecil

A thesis submitted to the Graduate Faculty of
Auburn University
in partial fulfillment of the
requirements for the Degree of
Master of Science

Auburn, Alabama
August 6, 2016

Keywords: solid rocket motor, hybrid rocket engine, compressibility, Trkalian, swirling flow

Approved by

Joseph Majdalani, Chair, Professor and Francis Chair
Roy J. Hartfield, Walt and Virginia Woltosz Professor
Dudley S. Nichols, Research Associate Professor

Abstract

In this work, the bulk gaseous motion inside cylindrical chambers driven by wall normal injection with and without reactive headwalls is explored. The base model is of the Trkalian type and is here extended to include approximations for arbitrary headwall injection patterns as well as compressibility effects for an exact similarity conforming headwall injection profile. The inviscid, non-reacting, swirling flow model is first generalized to capture a variety of headwall injection patterns through the concept of orthogonality. This leads to an approximation with some error which is quantified in the analysis. The velocity and vorticity fields are characterized for four representative injection patterns including a similarity conforming injection profile in the form of a Bessel function. The exact similarity conforming injection profile is then used in the development of a compressible approximation. Dilational effects are captured through a compressible Brag–Hawthorne framework in conjunction with a Rayleigh-Janzen expansion. Here again, the velocity and vorticity fields are obtained, along with the pressure, density, and temperature. These field variables are then compared to the incompressible case as well as the compressible complex-lamellar solution without swirl. Furthermore, the sonic length which functions as a normalizing parameter is calculated for several specific heat ratios and injection coefficients.

Acknowledgments

I would like to acknowledge the tremendous support of my family and friends during the journey of conducting the research that has resulted in this thesis. I feel that a special thank you to my parents is warranted for their constant encouragement and guidance that has helped me navigate life in such a way that this accomplishment was possible. Furthermore, I would like to thank Dr. Majdalani for his instruction and advice in the preparation of this thesis and during the research process.

Table of Contents

List of Figures

List of Tables

List of Symbols

a	chamber radius
B	normalized tangential angular momentum, $\bar{B}/(aU_w)$
c_n	swirl momentum constants, $n \in [0, 3]$
D^2	axisymmetric Stoke's operator
H	normalized stagnation head, $\bar{H}/U_w^2$
$\mathcal{I}_{h,n}, \mathcal{I}_m$	headwall injection integral or compressible integral where $m \in [1, 12]$
J_n, Y_n	nth order Bessel function of the first and second kind
k_n	integration constant where $n \in [1, 12]$
L	chamber length
l	aspect ratio, L/a
L_s	sonic length
M_w	wall injection Mach number
p	normalized pressure, $\bar{p}/p_0$

p_0	reference pressure
Q_r, Q_θ, Q_z	vorticity transport equation residual components
r, z	normalized radial and axial coordinates, $(\bar{r}, \bar{z})/a$
Re	Reynolds number
S_n	series where $n \in [1, 6]$
T	temperature
U_c	centerline headwall injection velocity
u_c	normalized centerline injection velocity, U_c/U_w
u_h	headwall injection constant, $u_c J_1(\lambda_1)/\lambda_1$
u_r, u_θ, u_z	normalized radial, tangential, and axial velocities, $(\bar{u}_r, \bar{u}_\theta, \bar{u}_z)/U_w$
U_w	radial injection velocity

Greek

γ	ratio of specific heats
ϵ	small perturbation parameter
θ	tangential coordinate
λ_n	nth zero of the zeroth order Bessel function of the first kind
ν	kinematic viscosity

ρ	normalized density, ρ/ρ_0
ρ_0	reference density
ψ	normalized streamfunction, $\bar{\psi}/(\rho_0 a U_w^2)$
$\boldsymbol{\omega}$	vorticity vector
∇	gradient operator

Abbreviations and Acronyms

BHE	Bragg-Hawthorne Equation
HRE	hybrid rocket engine
SRM	solid rocket motor
VTE	vorticity transport equation

Subscripts and Superscripts

$0, 1, 2, ...$	perturbation order
$\bar{\ }$	overbars denote dimensional quantities
$\tilde{\ }$	viscously corrected
c	centerline value
w	wall value

Chapter 1

Introduction

1.1 Background

The Taylor-Culick profile[1] has long been perceived as the standard approximation for the mean flowfield in solid rocket motors (SRMs), where it has been introduced in the context of steady, rotational, axisymmetric, inviscid, and incompressible motion. Due to the simplicity of its expression and its pseudo-viscous disposition to satisfy the no-slip condition at the propellant sidewall, it has been used at the foundation of a large number of investigations aimed at describing acoustic wave disturbances (Flandro et al. [2] and Fischbach et al. [3, 4]), particle-mean flow interactions (Féraille and Casalis [5], Bhatia et al. [6], and Féraille et al. [7]), and both vorticoacoustic and hydrodynamic instabilities in SRMs (Ugurtas et al. [8], Fabignon et al. [9], and Boyer et al. [10, 11]), where it has been relied upon to represent the bulk gaseous motion. According to this traditional model, the steady-state velocity and vorticity distributions remain strictly orthogonal, thus giving rise to the onset of complex lamellar vector fields [12]. Nonetheless, based on the underlying assumptions that stand behind its fundamental derivation, no swirl component of the mean flow velocity is permitted to evolve. This feature limits its applicability to studies conducted in circular-port rocket motors with right-cylindrical, internal burning grains, where the flowfield has often been reported to develop an intrinsic tendency to swirl, as shown by Dunlap et al. [13, 14] and Balachandar et al. [15] (see Fig. 1.1).

In seeking incremental improvements to the Taylor-Culick profile, several studies may be worthwhile to mention. Majdalani and Akiki [16], Xu et al. [17], and Majdalani et al. [18, 19] modify the base flow to capture the effects of viscous shear layers and receding grain surfaces; Kurdyumov [20] uses a semi-analytical approach to account for the effects of non-circular cross-sections; Majdalani [21] and Maicke and Majdalani [22] employ a Rayleigh-Janzen expansion to predict its behavior under high speed flow conditions; and Majdalani and Saad [23] as well as Saad and Majdalani [24] allow the solution to accommodate arbitrary headwall injection in the cylindrical and slab cases, respectively. Then by assuming a slender, wall-injecting motor, Traineau et al. [25], Balakrishnan et al. [26], and Akiki and Majdalani [27, 28]

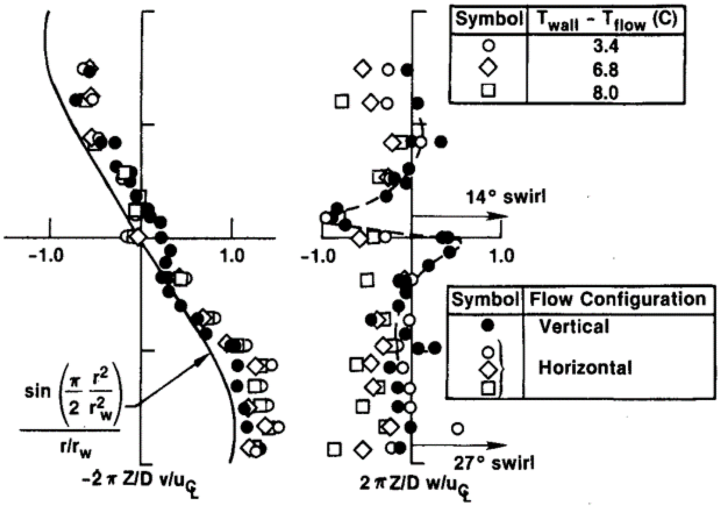

Figure 1.1. Evidence of a finite swirl-velocity according to the three element hot wire measurements acquired in the classical experiments conducted by Dunlap et al. [13] at the Chemical Systems Division (CSD) of United Technologies. Results show their radial v and tangential w velocities normalized by our $\bar{u}_z(0,\bar{z})/(\pi z)$. Courtesy of Dunlap et al. [13].

reduce the compressible Euler equations to a single integral equation that can be solved straightforwardly in the presence of either uniform or non-uniform wall fluxes.

More recently the Bragg-Hawthorne equation (BHE) has been revisited by Majdalani [12] because of the freedom that it affords in the choice of specific representations of the total fluid head and angular momentum, namely, to produce realistic, swirl capable solutions. For example, by choosing a constant angular momentum and total head that varies with the square of the stream function, the traditional Taylor-Culick profile may be recovered as a special case of the Bragg-Hawthorne formulation, wherein swirl is forcefully suppressed. Majdalani and Fist [29] make use of the freedom granted by the Bragg-Hawthorne framework by specifying more realistic relations for the total fluid head and angular momentum, hence leading to a Trkalian profile in which the vorticity and velocity fields remain parallel everywhere. According to the so-called Majdalani-Fist profile, a swirl component is permitted to freely develop, thus explaining several reported observations of swirling mean flow motions in simulated SRMs.

However, among the studies surveyed so far, the majority of developments retain a focus on SRMs with inert headwalls or similarity-conforming headwall injection profiles that can simplistically mimic the effects of reacting headwalls. In the case of hybrid rocket engines (HREs), where the headwall injection of an oxidizer stream becomes a dominant feature of the flowfield, or SRMs with complex grain shapes at their forward closures, studies mentioned earlier, namely, an axisymmetric study by Majdalani and Saad [23] followed with a planar formulation by Saad and Majdalani [24], have been helpful at reconstructing the TC model for internal burning cylinders and slab chambers in the presence of arbitrary headwall injection patterns. Therefore, by adopting a similar strategy, the focus of the first half of this thesis will be to reconstruct the incompressible Trkalian motion [29] while extending it to both SRMs and HREs with arbitrary headwall injection and a swirling flowfield.

In addition, and as alluded to earlier, among the available high speed flow models of the bulk gaseous motion in SRMs and HREs, one may identify the compressible counterpart of the non-swirling Taylor-Culick profile for both cylindrical [21] and slab [22] rocket motors. Both of these solutions stem from a Rayleigh-Janzen expansion of the vorticity-stream function equations using axisymmetric cylindrical and planar Cartesian coordinates, respectively. In this manner, compressible solutions are obtained that are essentially two-dimensional, i.e., where a transverse or swirl component of the velocity is not allowed to develop, especially in the cylindrical rocket case. Among its basic features, the Rayleigh-Janzen expansion enables us to identically recover the incompressible Taylor-Culick profile at leading order with compressible corrections that appear at first and subsequent orders in the wall Mach number squared, and where the bulk dilatational effects are encapsulated within the first order correction. However, in pursuing a compressible model in which swirl is exhibited, the vorticity-stream function approach must be abandoned, as it can only be effective in the treatment of a problem with two velocity components. In the presence of three velocity components, and in an effort to avoid suppressing swirl artificially, the more general Bragg-Hawthorne formulation must be employed.

In the pursuit of a compressible solution for the bidirectional vortex, Maicke and Majdalani [30] have developed a well-posed compressible Bragg-Hawthorne framework in which a Rayleigh-Janzen expansion is systematically unraveled. The corresponding procedure consists of sequentially solving the problem's conservation equations to the extent of producing an analytical approximation for the compressible motion under axisymmetric, inviscid, and isentropic flow conditions. This procedure was successfully employed by Maicke and Majdalani [31] in their effort at deriving the compressible flow analog of the bidirectional vortex in the context of a cyclonically-driven liquid rocket engine. Following their formulation and the specifics of the Trkalian profile [29], the main objective of the second half of this thesis will be to develop a compressible approximation for the bulk gaseous swirling motion in the context of a cylindrically-shaped, internal burning SRM or HRE, where a similarity conforming headwall injection profile may be accounted for.

Procedurally, the paper is organized as follows. First, the geometry, normalized variables, and boundary conditions which are common to both parts are presented. The effort to capture arbitrary inlet profiles begins in Chapter 2 with the normalized Bragg-Hawthorne equation and the boundary conditions recast in terms of the streamfunction. The resulting partial differential equation is then separated and solved using a Bessel-Fourier series approach that may be used to capture the effects of arbitrary headwall functions. In Sec. 2.2, the effects of varying the inlet profiles on the streamlines, velocity distributions, and vorticity fields are thoroughly examined as well as expressions for the residual that can accrue in the resulting series approximations. At this point, a finite volume solver is employed to provide point-by-point verifications of the velocity field. Due to a spurious singularity in the residual error calculation, we then proceed to develop in Sec. 2.3 a viscous correction for the tangential velocity at the sidewall using the tools of matched asymptotic expansions. The convergence of the residual error is subsequently confirmed while rigorous proofs for each of the summation series of interest are relegated to an Appendix. Finally, to close the discussion of discretionary headwall injection, a summary of our conclusions is provided in Sec. 2.4.

Chapter 3 begins with a presentation of the compressible Bragg-Hawthorne framework as developed by Maicke and Majdalani [30]. A Rayleigh-Janzen perturbation solution is then sought in which the boundary conditions are carefully treated in Sec. 3.2 and results for leading and first order equations presented in Secs. 3.3–3.4. The velocity field is examined and compared to its Taylor-Culick analog in Sec. 3.5.1 along with the thermodynamic variables in Sec. 3.5.2 and the distance at which sonic conditions are achieved in Sec. 3.5.3. Furthermore, the sonic length is then used as a normalizing parameter for the further characterization of the flowfield velocities in Sec. 3.5.4. Finally, the results of the compressible study are summarized and concluded in Sec. 3.6

1.2 Problem Setup

1.2.1 Geometric Configuration

The problem in question is that of the bulk gaseous motion in a cylindrical grain under the assumptions of axisymmetric, steady, rotational, single-phase, non-reactive, inviscid, and either incompressible or compressible flow. We idealize the

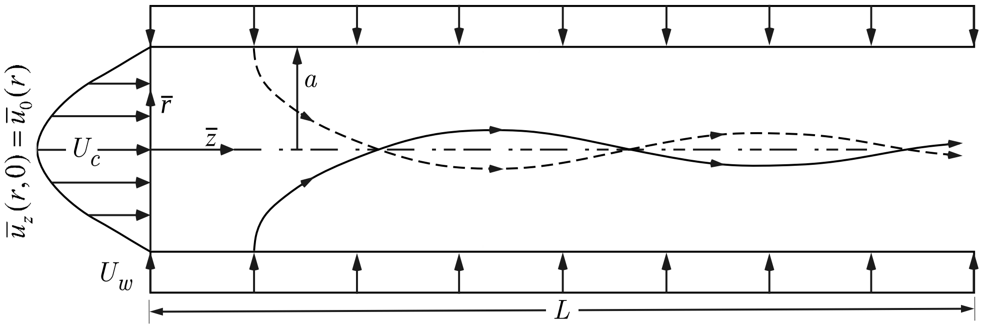

Figure 1.2. Schematic of a right-cylindrical, internal burning rocket with a similarity-conforming, headwall injection profile.

rocket as a porous enclosure with a nozzleless aft end as seen in Fig. 1.2. The radial, tangential, and axial velocities are represented by $(\bar{u}_r, \bar{u}_\theta, \bar{u}_z)$ and the spatial coordinates by $(\bar{r}, \bar{\theta}, \bar{z})$, where overbars denote dimensional quantities. The headwall injection velocity at the centerline is denoted by $U_c = \bar{u}_z(0,0)$, and the chamber radius and length are given by a and L. Note that U_c can be chosen to reproduce a comparable mass flow rate to that arising at the forward closure of a solid rocket motor, or the injector faceplate of a hybrid rocket engine. This can be accomplished by ensuring that the same mass flux is produced at the chamber headwall as that occurring in the actual motor. Along similar lines, U_w may be taken to be representative of the blowing velocity generated by the burnback of a solid propellant, or the regression rate of a hybrid fuel grain.

1.2.2 Normalization

Using the chamber radius a and the sidewall injection speed U_w as reference values, all primary variables can be made dimensionless according to

$$\begin{aligned} &z = \frac{\bar{z}}{a};\ r = \frac{\bar{r}}{a};\ l = \frac{L}{a};\ \nabla = a\bar{\nabla};\ u_c = \frac{U_c}{U_w}\ u_r = \frac{\bar{u}_r}{U_w};\ u_\theta = \frac{\bar{u}_\theta}{U_w};\\ &u_z = \frac{\bar{u}_z}{U_w};\ \boldsymbol{\omega} = \frac{a\bar{\boldsymbol{\omega}}}{U_w};\ \psi = \frac{\bar{\psi}}{\rho_0 U_w a^2};\ H = \frac{\bar{H}}{U_w^2};\ B = \frac{\bar{B}}{aU_w};\ p = \frac{\bar{p}}{p_0};\ \rho = \frac{\bar{\rho}}{\rho_0} \end{aligned} \tag{1.1}$$

where p_0 and ρ_0 designate the reference pressure and density. It should be noted that for a solid rocket motor, when the same propellant type occupies both the headwall and sidewall grain regions, the value of u_c will ensure that the same mass flux at $z = 0$ is produced, which can be found through a simple mass balance given by

$$\int_0^1 u_0(r) r \mathrm{d}r = \frac{1}{2} \tag{1.2}$$

where u_c is embedded in the arbitrary injection function $u_0(r)$. Conversely, the headwall injection constant associated with hybrid rockets can be quite large, especially that the sidewall injection velocity U_w, which scales with the inert fuel regression rate, can be appreciably smaller than U_c; the latter is generally prescribed by the fast incoming oxidizer stream and the ratio of headwall-to-sidewall propellant densities.

1.2.3 Boundary Conditions

The boundary conditions that accompany the model of a SRM or HRE may be attributed to axisymmetry, uniform wall-normal injection, a user-specified headwall injection profile, and a vanishing tangential velocity at the center of the headwall. In conjunction with the geometric configuration at hand, these requirements translate into

(a) a vanishing radial velocity along the centerline: $u_r(0, z) = 0$;

(b) uniform injection along the sidewalls: $u_r(1, z) = -1$;

(c) an enforcement of the no-slip condition on the axial velocity along the sidewall: $u_z(1, z) = 0$;

(d) an arbitrary injection pattern at the headwall: $u_z(r, 0) = u_0(r)$; and

(e) a swirl velocity that vanishes at the headwall center: $u_\theta(0, 0) = 0$.

With the common geometry, normalization, and boundary conditions established the two specific cases of interest will be explored. In Chapter 2, the incompressible form of the Bragg-Hawthorne equation will serve as the starting point for developing a generalized Trkalian flowfield which captures the effects of a user imposed inlet profile at the headwall. Chapter 3 will then introduce the compressible Bragg-Hawthorne equation from which an asymptotic solution that captures dilatational effects will be presented.

Chapter 2

Arbitrary Headwall Injection

2.1 Formulation

2.1.1 Incompressible Governing Equation and Boundary Conditions

Using the normalized variables of Eq. (1.1), the Bragg-Hawthorne equation [32], which represents a special form of Euler's equation for axisymmetric, steady, and incompressible flows, may be written as

$$\frac{\partial^2\psi}{\partial r^2} - \frac{1}{r}\frac{\partial\psi}{\partial r} + \frac{\partial^2\psi}{\partial z^2} = r^2\frac{\mathrm{d}H}{\mathrm{d}\psi} - B\frac{\mathrm{d}B}{\mathrm{d}\psi} \tag{2.1}$$

Subsequently, in making use of the incompressible Stokes streamfunction,

$$u_r = -\frac{1}{r}\frac{\partial\psi}{\partial z}, \qquad u_z = \frac{1}{r}\frac{\partial\psi}{\partial r} \tag{2.2}$$

the boundary conditions presented in Sec. 1.2.3 may be conveniently converted into

$$-\frac{1}{r}\frac{\partial \psi}{\partial z}\bigg|_{(0,z)} = 0 \qquad \text{(no radial flow across centerline)} \tag{2.3}$$

$$-\frac{1}{r}\frac{\partial \psi}{\partial z}\bigg|_{(1,z)} = -1 \qquad \text{(radial velocity at the sidewall)} \tag{2.4}$$

$$\frac{1}{r}\frac{\partial \psi}{\partial r}\bigg|_{(1,z)} = 0 \qquad \text{(no axial slip at the sidewall)} \tag{2.5}$$

$$\frac{1}{r}\frac{\partial \psi}{\partial r}\bigg|_{(r,0)} = u_0(r) \qquad \text{(prescribed headwall injection)} \tag{2.6}$$

$$\frac{1}{r}B(\psi)\bigg|_{(0,0)} = 0 \qquad \text{(no swirl velocity at headwall center)} \tag{2.7}$$

Next, B and H may be specified according to Majdalani and Fist [29] in order to precipitate solutions that belong to the same Trkalian family of self-similar flows as before. The particular Trkalian motion may be achieved by prescribing a constant stagnation head and a tangential angular momentum relation with the streamfunction that correspond to

$$\frac{\mathrm{d}H}{\mathrm{d}\psi} = 0 \qquad \text{and} \qquad B\frac{\mathrm{d}B}{\mathrm{d}\psi} = c_0^2\psi, \quad \text{hence} \quad B = \sqrt{c_0^2\psi^2 + c_1^2} \tag{2.8}$$

Substituting these expressions into Eq. (3.4) yields

$$\frac{\partial^2 \psi}{\partial r^2} - \frac{1}{r}\frac{\partial \psi}{\partial r} + \frac{\partial^2 \psi}{\partial z^2} + c_0^2\psi = 0 \tag{2.9}$$

2.1.2 Solution Method

Equation (2.9) may be readily separated using $\psi(r,z)=f(r)g(z)$, a form that unravels three possible outcomes:

$$-\frac{\ddot{g}(z)}{g(z)}=\frac{1}{f}\left(f''-\frac{1}{r}f'+c_0^2 f\right)=\begin{cases}0 & \text{(type 0)}\\ +\nu^2 & \text{(type I)}\\ -\nu^2 & \text{(type II)}\end{cases} \tag{2.10}$$

In previous work [29], only the type 0 case in Eq. (2.10) is considered, thus leading to

$$\psi(r,z)=r\left(z+u_h\right)J_1(\lambda_n r);\quad u_h\equiv u_c J_1(\lambda_1)/\lambda_1 \tag{2.11}$$

where λ_n remains limited to λ_1, the first zero of the zeroth order Bessel function of the first kind. Such an approach restricts the analysis to a partial solution that is capable of capturing the mean flow with either no headwall injection, or with a similarity-conforming Bessel function at $z=0$. Since we presently seek to extend the formulation to encompass arbitrary injection profiles, we take advantage of the linearity of Eq. (2.9) and superimpose all possible partial solutions. Clearly, a summation over all λ_n will enable us to capture a wider variety of headwall injection profiles that may be appropriate of SRM and HRE inlet patterns. We also examine the viability of the type I and II solutions vis-à-vis the problem's fundamental set of boundary conditions. Based on Eq. (2.10), we recover

$$\psi(r,z)=\begin{cases} r\,(k_1 z+k_2)\,[k_3 J_1(c_0 r)+k_4 Y_1(c_0 r)] & \text{(type 0)}\\ r\,[k_1\sin(\nu z)+k_2\cos(\nu z)] & \\ \quad\times\left[k_3 J_1(r\sqrt{c_0^2-\nu^2})+k_4 Y_1(r\sqrt{c_0^2-\nu^2})\right] & \text{(type I)}\\ r\,[k_1\sinh(\nu z)+k_2\cosh(\nu z)] & \\ \quad\times\left[k_3 J_1(r\sqrt{c_0^2+\nu^2})+k_4 Y_1(r\sqrt{c_0^2+\nu^2})\right] & \text{(type II)} \end{cases} \tag{2.12}$$

The next step is to secure the problem's boundary conditions. First, to avoid singularities as $r \to 0$ in the process of satisfying condition (a) or Eq. (3.14), we take $k_4 = 0$ and reduce the above expressions into

$$\psi(r,z)=\begin{cases} r\,(K_1 z+K_2)\,J_1(c_0 r) & \text{(type 0)}\\ r\,[K_1\sin(\nu z)+K_2\cos(\nu z)]\,J_1(r\sqrt{c_0^2-\nu^2}) & \text{(type I)}\\ r\,[K_1\sinh(\nu z)+K_2\cosh(\nu z)]\,J_1(r\sqrt{c_0^2+\nu^2}) & \text{(type II)} \end{cases} \tag{2.13}$$

where $K_1 = k_1 k_3$ and $K_2 = k_2 k_3$. Second, applying the axial no-slip condition (c) or Eq. (3.16), we obtain

$$\left.\begin{array}{l} J_0(c_0)\\ J_0(\sqrt{c_0^2-\nu^2})\\ J_0(\sqrt{c_0^2+\nu^2}) \end{array}\right\}=0 \quad \text{or} \quad \begin{cases} c_0=\lambda_n & \text{(type 0)}\\ \nu_n=\sqrt{c_0^2-\lambda_n^2} & \text{(type I)}\\ \nu_n^*=\sqrt{\lambda_n^2-c_0^2} & \text{(type II)} \end{cases} \tag{2.14}$$

Third, as we seek to capture an arbitrary injection profile at the headwall, we take advantage of superposition and write

$$u_z(r,0) = u_0(r) = \sum_{n=1}^{\infty} K_{2,n} \lambda_n J_0(\lambda_n) \tag{2.15}$$

The orthogonality principle may then be applied to extract each of the $K_{2,n}$ coefficients from the well-defined integral

$$K_{2,n} = \frac{2}{\lambda_n J_1^2(\lambda_n)} \int_0^1 r u_0(r) J_0(\lambda_n r) \mathrm{d}r \tag{2.16}$$

At this juncture, we may impose the radial injection condition in Eq. (3.15) by setting

$$u_r(1,z) = 1 = \begin{cases} \displaystyle\sum_{n=1}^{\infty} K_{1,n} J_1(\lambda_n) & \text{(type 0)} \\ \displaystyle\sum_{n=1}^{\infty} \sqrt{c_0^2 - \lambda_n^2} \Big[K_{1,n} \cos(z\sqrt{c_0^2 - \lambda_n^2}) & \\ \qquad -K_{2,n} \sin(z\sqrt{c_0^2 - \lambda_n^2}) \Big] J_1(\lambda_n) & \text{(type I)} \\ \displaystyle\sum_{n=1}^{\infty} \sqrt{\lambda_n^2 - c_0^2} \Big[K_{1,n} \cosh(z\sqrt{\lambda_n^2 - c_0^2}) & \\ \qquad -K_{2,n} \sinh(z\sqrt{c_0^2 - \lambda_n^2}) \Big] J_1(\lambda_n) & \text{(type II)} \end{cases} \tag{2.17}$$

Upon closer scrutiny, it may be realized that the type I and II solutions do not offer viable alternatives. For example, in order to satisfy their forms in Eq. (2.17) for all z, both ν_n and ν_n^* must be artificially chosen such that the length of the chamber is made to correspond to a quarter period of an odd function[1] that is suitable for describing the sidewall injection pattern along the length of the chamber. Orthogonality could then be applied to extract $K_{1,n}$. However, the sinusoidal variation in the axial direction does not lend itself to a physical solution because it does not allow for the gradual growth of the axial velocity in the streamwise direction as mass is continually added along the sidewall. Owing to these considerations, we return to the well-behaved type 0 solution, which varies linearly in the axial direction. In this case, Eq. (2.17) yields

$$K_{1,n} = \begin{cases} \dfrac{1}{J_1(\lambda_n)} & n = 1 \\ \\ 0 & n \neq 1 \end{cases} \tag{2.18}$$

Finally, by enforcing condition (e) or Eq. (3.18), we deduce $c_1 = 0$ and therefore $B = \lambda_n \psi$ in Eq. (2.8). The ensuing streamfunction and velocity expressions reduce to

$$\psi(r,z) = r\left\{\left[z + \frac{2\mathcal{I}_{h,1}}{\lambda_1 J_1(\lambda_1)}\right]\frac{J_1(\lambda_1 r)}{J_1(\lambda_1)} + \sum_{n=2}^{\infty}\frac{2\mathcal{I}_{h,n} J_1(\lambda_n r)}{\lambda_n J_1^2(\lambda_n)}\right\} \tag{2.19}$$

$$u_r(r,z) = -\frac{J_1(\lambda_1 r)}{J_1(\lambda_1)} \tag{2.20}$$

$$u_z(r,z) = \left[\lambda_1 z + \frac{2\mathcal{I}_{h,1}}{J_1(\lambda_1)}\right]\frac{J_0(\lambda_1 r)}{J_1(\lambda_1)} + \sum_{n=2}^{\infty}\frac{2\mathcal{I}_{h,n} J_0(\lambda_n r)}{J_1^2(\lambda_n)} \tag{2.21}$$

$$u_\theta(r,z) = \left[\lambda_1 z + \frac{2\mathcal{I}_{h,1}}{J_1(\lambda_1)}\right]\frac{J_1(\lambda_1 r)}{J_1(\lambda_1)} + \sum_{n=2}^{\infty}\frac{2\mathcal{I}_{h,n} J_1(\lambda_n r)}{J_1^2(\lambda_n)} \tag{2.22}$$

---

[1] Since $K_{2,n}$ is used to satisfy the headwall injection condition, our Fourier type series is limited to cosine terms, thus restricting our sidewall injection profiles to those that can be defined as odd periodic functions.

where the headwall injection integral for an eigenmode n may be evaluated from

$$\mathcal{I}_{h,n} = \int_0^1 r u_0(r) J_0(\lambda_n r) \mathrm{d}r \tag{2.23}$$

2.1.3 Representative Headwall Injection Profiles

Up to this point, the formulation has been expressed in terms of an arbitrary headwall injection profile, $u_0(r)$. To make further headway, it is helpful to explicitly define several inlet profiles in order to examine their effects on the flow evolution. In retaining consistency with previous studies [23, 24], four increasingly blunter injection profiles are considered, namely,

$$u_0(r) = \begin{cases} u_c J_1(\lambda_1 r) & \text{self similar} \\ u_c(1 - r^2) & \text{Poiseuille} \\ u_c(1 - r^4) & \text{pseudo cosine} \\ u_c(1 - r^8) & \text{power law} \end{cases} \tag{2.24}$$

Each of these profiles can be substituted into Eq. (2.23) to obtain closed-form analytical expressions for $\mathcal{I}_{h,n}$. Naturally, the similarity-conforming case leads to an exact solution for which no summation is necessary [29]. The remaining three profiles yield the simple relations given by

$$\mathcal{I}_{h,n} = \begin{cases} \dfrac{4u_c J_1(\lambda_n)}{\lambda_n^3} & \text{Poiseuille} \\ \dfrac{u_c J_1(\lambda_n)}{\lambda_n^5}\left(16\lambda_n^2 - 64\right) & \text{pseudo cosine} \\ \dfrac{u_c J_1(\lambda_n)}{\lambda_n^9}\left(64\lambda_n^6 - 2304\lambda_n^4 + 36864\lambda_n^2 - 147456\right) & \text{power law} \end{cases} \tag{2.25}$$

In order to specify u_c, the problem of a cylindrical SRM with the same propellant composition occupying both headwall and sidewall regions may be considered. In this configuration, the centerline injection speed u_c may be taken to correspond to a headwall grain that exhibits the same burning rate as that of the sidewall. It can hence be determined by equating the mass flow rate of the arbitrary profile to that of a uniformly burning propellant occupying the same circular cross section at $z = 0$. The ensuing mass balance yields

$$\int_0^1 r u_0(r)\mathrm{d}r = \frac{1}{2} \tag{2.26}$$

and so

$$u_c = \begin{cases} 2.316 \quad \left[\text{i.e., } \tfrac{1}{2}\lambda_1/J_1(\lambda_1)\right] & \text{self similar} \\ 2 & \text{Poiseuille} \\ 1.5 & \text{pseudo cosine} \\ 1.25 & \text{power law} \end{cases} \tag{2.27}$$

While the above values correspond to a headwall burning grain in a cylindrical SRM, u_c may be increased by roughly one order of magnitude when accounting for the oxidizer-to-fuel speed magnification that would be appropriate of a cylindrical HRE flowfield (see also Abu-Irshaid et al. [34]).

2.2 Flowfield Characterization

In what follows, the effects of varying the headwall injection pattern on both velocity and vorticity fields are explored. In this process, the velocity evolution in the chamber is compared to numerical simulations obtained using a finite volume solver. We also examine the behavior of the residual error, which is entailed in the vorticity transport equation, for cases in which the superposition of partial solutions does not yield an exact outcome but rather leads to an approximate series representation.

2.2.1 Velocities

Based on the inlet profiles defined in Sec. 2.1.3, the evolution of the axial and tangential velocities may be characterized throughout the chamber. As for the radial velocity, which is given by Eq. (2.20), it may be readily verified that its expression remains axially invariant and independent of the headwall injection profile.

In the spirit of standardizing visual illustrations and later comparisons to numerical simulations, and despite the self-similar and non-dimensional nature of our formulation, we find it helpful to assume a chamber aspect ratio of $l = 10$, which can be realized, for example, using a length of 1 m and a radius of 0.1 m. Moreover, before delving into spatial distributions of the velocity and vorticity fields, it may be useful to depict in Fig. 2.1a the four representative headwall injection velocity patterns at $z = 0$. This is followed in Fig. 2.1b with the axial profiles that develop at $z = 10$, or ten radii downstream of the chamber's headwall boundary. We also display in Fig. 2.1b the self similar u_z with no headwall injection (hollow circles), as it constitutes the delimiting solution that all four cases will approach with successive increases in z. It may be immediately seen that despite the initially dissimilar spatial distributions of the four profiles at entry, they all seem to converge onto the exact similarity solution with an impermeable forward closure as the distance from the headwall is increased. Yet, as one would expect, the relative magnitudes of the centerline velocities of the four models, no matter how close, remain unchanged. For example, the similarity solution with a finite u_c retains the highest centerline speed throughout the chamber, with the other profiles following in succession according to their centerline values. Although this behavior may be bewildering at first, the tendency to converge back to the exact, self similar expression may be clarified by examining the velocity formulation given in Eqs. (2.21–2.22). In both u_z and u_θ expressions, the influence of the headwall injection pattern appears in the form of a radially varying perturbation series that remains independent of z, unlike the term

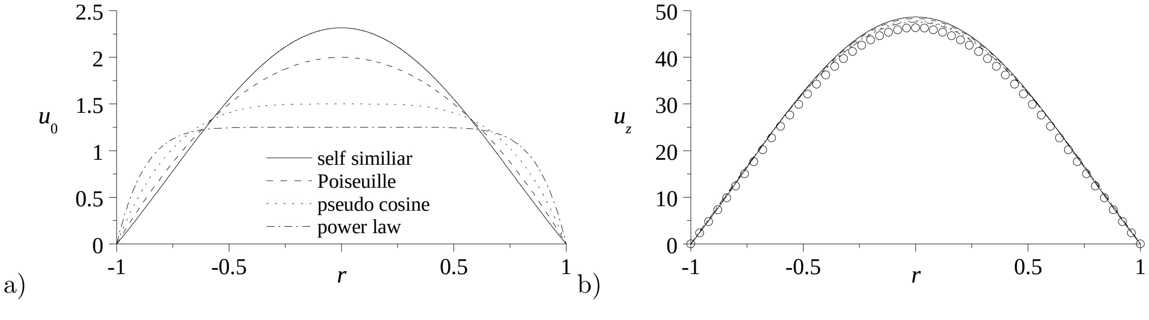

Figure 2.1. Axial velocity distributions associated with the four headwall injection profiles at a) $z = 0$ and b) $z = l = 10$. Here u_0 is defined according to Eq. (2.24) and Eq. (2.27). In Part b) , the exact solution for an impermeable headwall, to which all solutions will tend as $z \to \infty$, is depicted using hollow circles.

associated with the self similar solution. Hence, as z is increased, the relative contribution of the perturbation series, which is caused by a non-vanishing headwall injection profile, continues to diminish until it becomes immaterial in sufficiently long chambers. From a mathematical standpoint, the observed behavior may be confirmed by rewriting the axial velocity as $u_z = zg(r) + G(r)$, where $G(r)$ represents the summation terms produced by the inlet profile, and then by evaluating its magnitude relative to the exact solution with no headwall injection as z is enlarged. From Eq. (2.21), we have

$$g(r) = \lambda_1 \frac{J_0(\lambda_1 r)}{J_1(\lambda_1)} \tag{2.28}$$

$$G(r) = \sum_{n=1}^{\infty} \frac{2\mathcal{I}_{h,n} J_0(\lambda_n r)}{J_1^2(\lambda_n)} \tag{2.29}$$

Thus, in the limit as $z \to \infty$, the ratio of any axial velocity to the exact u_z with no headwall injection becomes

$$\lim_{z\to\infty} \frac{zg(r) + G(r)}{zg(r)} = \lim_{z\to\infty} \frac{g(r) + \frac{1}{z}G(r)}{g(r)} = 1 \tag{2.30}$$

which affirms the confluence of the profiles with the self similar case as z is increased. A similar analysis of the tangential velocity yields an identical outcome. Furthermore, this is an agreement with a study by Kurdyumov [35] which reaches a similar conclusion in the context of non-swirling Taylor-Culick flows.

Clearly, the deviation from the self similar solution with an impermeable headwall is controlled in large part by the centerline velocity, u_c. It can thus be argued that the injection pattern in HRE chambers will have a more significant impact on the flowfield development in the streamwise direction owing to its substantially larger u_c. Consequently, a much larger distance will be required in the case of hybrids before the self similar solution may be recovered. Furthermore, recalling that hybrid chambers are generally shorter than their SRM counterparts, the influence of user-specified headwall injection patterns on the developing flowfield character will be considerably more appreciable in HREs versus SRMs.

Using the u_c values determined by Eq. (2.27) and, hence, the low injection levels that are commensurate with reactive SRM headwall grains, the spatial evolution of u_z is illustrated in Fig. 2.2 at five equally spaced distances from the headwall and the four representative inflow cases defined in Eq. (2.24). For this modest level of injection, deviations that are attributed to a different initial profile at entry quickly disappear to the extent of becoming almost visually indistinguishable within 2.5 radii of the headwall.

Along similar lines, the tangential velocity evolution, which is illustrated in Fig. 2.3, exhibits a slightly different sensitivity. Here the increasingly blunter profiles lead to a monotonic increase in u_θ while moving radially outwardly until a maximum of $(u_\theta)_{\max}$ is reached near $r = 1$. This behavior is, however, limited to the vicinity of the headwall region where the peak tangential speed appears to be nearly touching the sidewall. As the flow progresses downstream, $(u_\theta)_{\max}$ continues to shift radially inwardly, and this leftward movement can be visually detected in Fig. 2.3 after approximately 2.5 radii. Thus, in the forward quarter of the chamber,

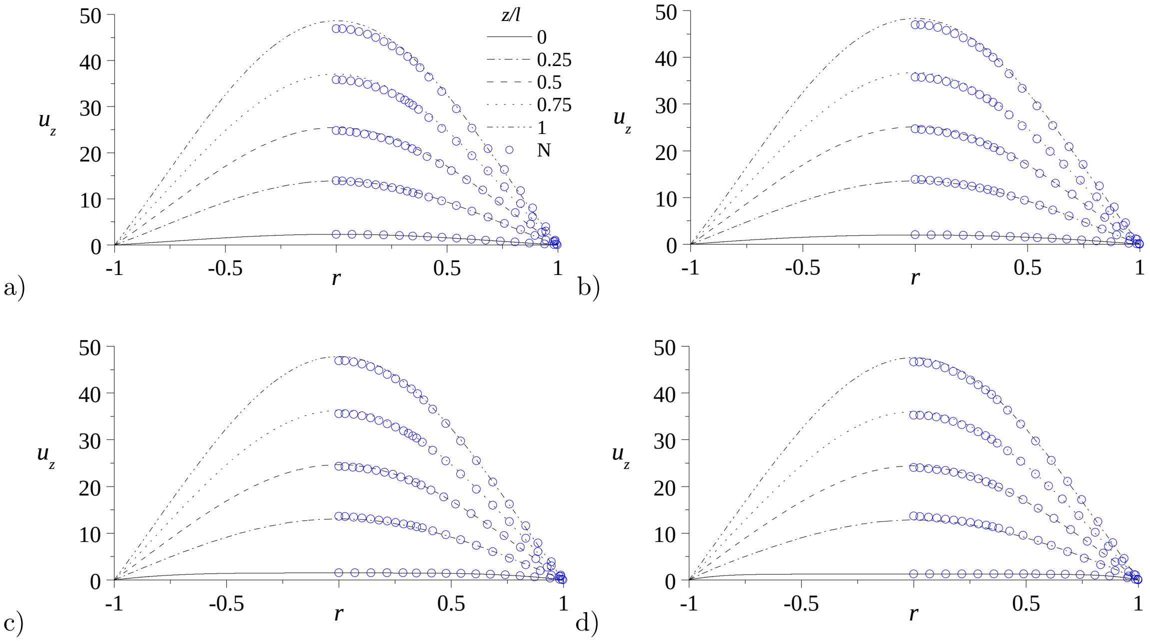

Figure 2.2. Analytical and numerical predictions of the axial velocity profiles at five axial stations corresponding to a) self similar, b) Poiseuille, c) pseudo cosine, and d) power law injection patterns at entry. Line plots describe the analytical solutions at different axial stations, whereas hollow circles denote numerical simulations using a finite volume solver.

the maximum tangential speed may be estimated from its sidewall value viz.

$$u_\theta|_{r=1} = \lambda_1 z + \sum_{n=1}^{\infty} \frac{2\mathcal{I}_{h,n}}{J_1(\lambda_n)} \tag{2.31}$$

The finite value of u_θ at the sidewall may be attributed to the inviscid nature of the solution allowing slip to occur at $r = 1$ unless a viscous wall correction is incorporated. It also affects the convergence property of the residual error at the sidewall. To overcome this deficiency, a wall boundary layer correction will be later pursued in Sec. 2.3 through the application of matched asymptotic expansion theory.

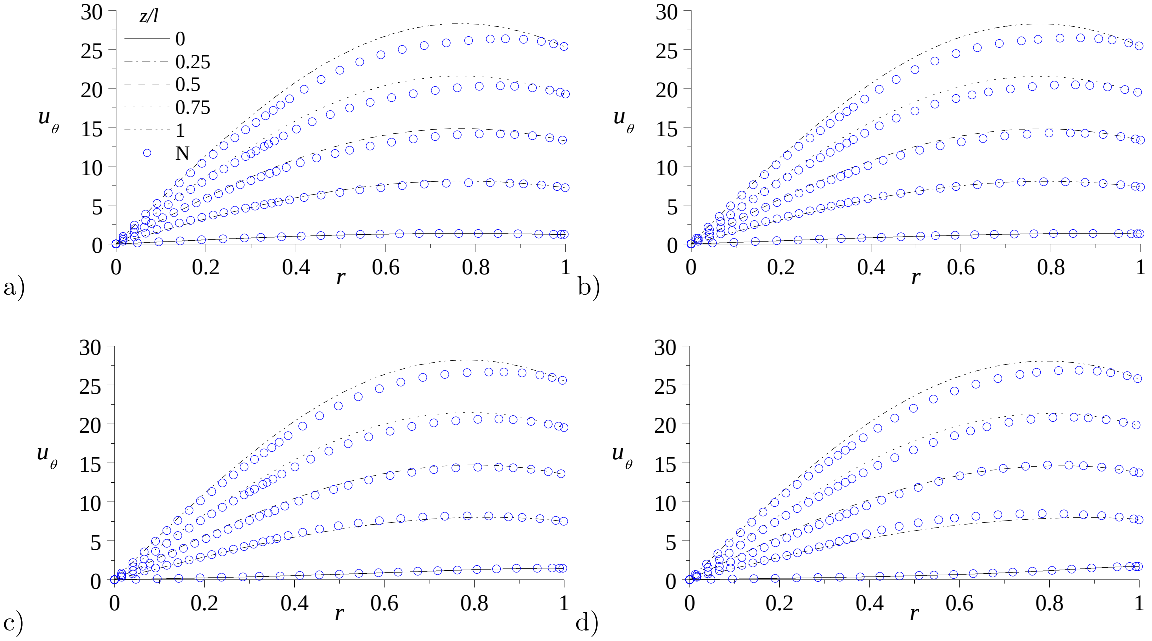

Figure 2.3. Analytical and numerical predictions of the tangential velocity profiles at five axial stations corresponding to a) self similar, b) Poiseuille, c) pseudo cosine, and d) power law injection patterns at entry. Line plots describe the analytical solutions at different axial stations, whereas hollow circles denote numerical simulations using a finite volume solver.

At this point, we turn out attention to the axially invariant radial velocity profile which is depicted in Fig. 2.4. Since u_r remains independent of both z and the initial injection profile at entry, the line plots corresponding to all four cases appear to be in perfect agreement. Here the radial velocity magnitude first increases from a value of unity at the sidewall, to a peak absolute value of $|u_r|_{\max} = 1.12$ at $r_{\min} = 0.7656$, before resuming its monotonic decrease to zero at the centerline. Although these results are consistent with those reported by Majdalani and Fist [29] or Majdalani and Saad [23, 21], a numerical simulation of the problem will be necessary to establish an independent avenue for verification.

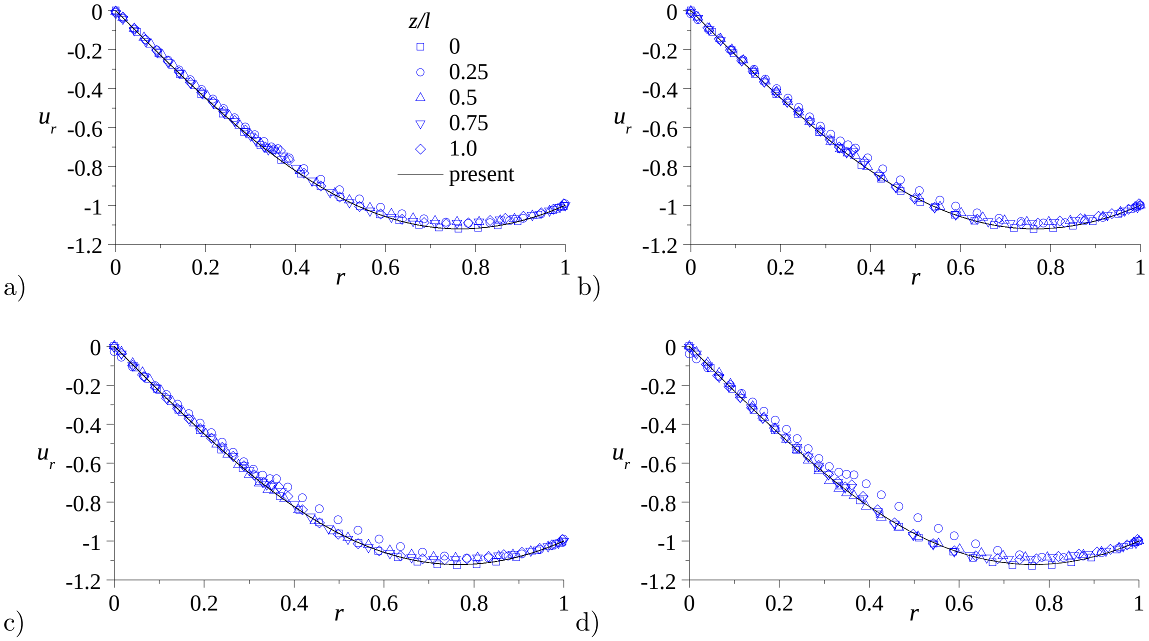

Figure 2.4. Analytical and numerical predictions of the radial velocity profiles at five axial stations corresponding to a) self similar, b) Poiseuille, c) pseudo cosine, and d) power law injection patterns at entry. The solid line refers to the spatially invariant analytical solution, whereas hollow symbols denote numerical simulations obtained at different axial stations.

2.2.2 Numerical Verification

In the interest of verifying our theoretical approximations, a finite volume solver, namely ANSYS Fluent 15.0, is used to perform inviscid simulations on a structured grid of 3,110,400 finite volume elements. Our geometry consists of a right-cylindrical tube of radius 0.1 m and length 1.6 m, thus extending a safe 0.6 m downstream of the specified domain size. The boundary conditions that we impose include the four axial injection profiles at the headwall as well as the radial and tangential conditions that arise in the problem at the fore end of the chamber. Along the sidewall, air as the working fluid is injected radially at 1 m/s and tangentially at a finite swirling speed that is consistent with the inviscid model at hand. As for the outlet, a pressure-outflow condition is prescribed at the aft end of the chamber. Procedurally, a pressure based solver is employed with the SIMPLE scheme to resolve pressure-velocity coupling along with the first order upwind method for momentum discretization. To expedite convergence, the solution is initialized using the present analytical formulations and simulations are subsequently continued until residuals have fallen below 10^{-3}.

Our computational results are overlaid in Figs. 2.2–2.4 using scattered lines of hollow circles that are intended to distinguish them from corresponding theoretical projections. When taking into account the approximate nature of the analytical expressions, it may be argued that the agreement between numerics and analytics is quite favorable in all three velocity components. This is especially true of the u_z simulations in Fig. 2.2 where spatial agreement is nearly perfect everywhere at first and then begins to very gradually deteriorate near the centerline as the distance from the headwall is increased. The opposite may be said of the tangential velocity in Fig. 2.3 where agreement with simulations is particularly strong near the centerline despite the small disparities that begin to emerge near the peak $(u_\theta)_{\max}$ values, especially as z is increased. As for the spatial invariance of the radial velocity, our findings in Fig. 2.4 confirm that computational estimates at five equispaced locations collapse onto a single curve, which is accurately predicted by the present theory, especially for the similarity-conforming case where deviations from theory are virtually absent. For the Poiseuille, pseudo cosine, and power law profiles, very minute deviations from the analytical u_r seem to appear around $r = 0.5$ and $z = 0.25$, only to vanish as the flow is further developed. Overall, these finite volume computations lend support to the accuracy and viability of the present formulations despite the somewhat complex error residuals that accrue during their establishment.

2.2.3 Vorticity and Streamlines

With the velocities being well established, the vorticity may be readily evaluated. In cylindrical coordinates under axisymmetric conditions, we have

$$\boldsymbol{\omega} = \nabla \times \boldsymbol{u} = -\frac{\partial u_\theta}{\partial z}\hat{\boldsymbol{e}}_{\boldsymbol{r}} + \left(\frac{\partial u_r}{\partial z} - \frac{\partial u_z}{\partial r}\right)\hat{\boldsymbol{e}}_{\boldsymbol{\theta}} + \frac{1}{r}\frac{\partial\left(r u_\theta\right)}{\partial r}\hat{\boldsymbol{e}}_{\boldsymbol{z}} \tag{2.32}$$

After carefully extracting spatial derivatives and grouping, we obtain

$$\begin{aligned}\boldsymbol{\omega} = -\frac{\lambda_1 J_1(\lambda_1 r)}{J_1(\lambda_1)}\hat{\boldsymbol{e}}_{\boldsymbol{r}} &+ \left\{\left[\lambda_1 z + \frac{2\mathcal{I}_{h,1}}{J_1(\lambda_1)}\right]\frac{\lambda_1 J_1(\lambda_1 r)}{J_1(\lambda_1)} + \sum_{n=2}^{\infty}\frac{2\lambda_n \mathcal{I}_{h,n} J_1(\lambda_n r)}{J_1^2(\lambda_n)}\right\}\hat{\boldsymbol{e}}_{\boldsymbol{\theta}} \\ &+ \left\{\left[\lambda_1 z + \frac{2\mathcal{I}_{h,1}}{J_1(\lambda_1)}\right]\frac{\lambda_1 J_0(\lambda_1 r)}{J_1(\lambda_1)} + \sum_{n=2}^{\infty}\frac{2\lambda_n \mathcal{I}_{h,n} J_0(\lambda_n r)}{J_1^2(\lambda_n)}\right\}\hat{\boldsymbol{e}}_{\boldsymbol{z}}\end{aligned} \tag{2.33}$$

In the above, one may almost glean the Trkalian nature of the flowfield, which is prescribed by the condition $\boldsymbol{\omega} = \lambda_1 \boldsymbol{u}$, were it not for the error caused by the series summation over many eigenvalues. In fact, it may be easily seen that the masking of the Trkalian nature is gradually lifted as $z \to \infty$. Here again, consistently with the velocity character, the radial vorticity remains axially invariant and independent of the profile at entry. Since $\omega_r = \lambda_1 u_r$, its graphical representations will mirror Fig. 2.4 and are therefore omitted.

We proceed by exploring the axial component of vorticity in Fig. 2.5 for the four injection profiles at equally spaced stations along the chamber length. In the headwall region, it may be interesting to note that ω_z will first increase and then slowly diminish as it approaches the centerline inwardly and that the drop becomes more appreciable going from Fig. 2.5a to Fig. 2.5d, i.e., as the inlet profile becomes blunter. This behavior may be partly attributed to the decreased tangential velocity gradient in the radial direction as reflected in Fig. 2.3. Graphically, and consistently with our earlier observation, a breakdown in the Trkalian nature of the flowfield, which should otherwise predict a mirroring between axial velocity and vorticity plots, may be identified in the headwall region where the specific injection pattern remains dominant. The slight dissimilarities between u_z and ω_z also become more pronounced with further departures from the similarity-conforming inlet profile.

The tangential component of vorticity pictured in Fig. 2.6 proves equally interesting, thus illustrating the minor departures from the Trkalian nature of the base flow in the first quarter of the chamber. In conjunction with the blunter injection profiles, ω_θ remains negligibly small for much of the central portion of the chamber. While a flattening of u_θ in the core region is identified in Fig. 2.3, the corresponding vorticity steepening is even more pronounced as we transition from Fig. 2.6a to Fig. 2.6d. Also pictured in Fig. 2.6 is the vorticity associated with the extended Taylor-Culick motion [23] for the same injection patterns except for the self similar case where the TC model employs a half cosine inlet profile. Having only axial and radial components of velocity, the TC model gives rise to a tangential component of vorticity only. At $z = 0$ both the TC and Trkalian vorticities seem to match and

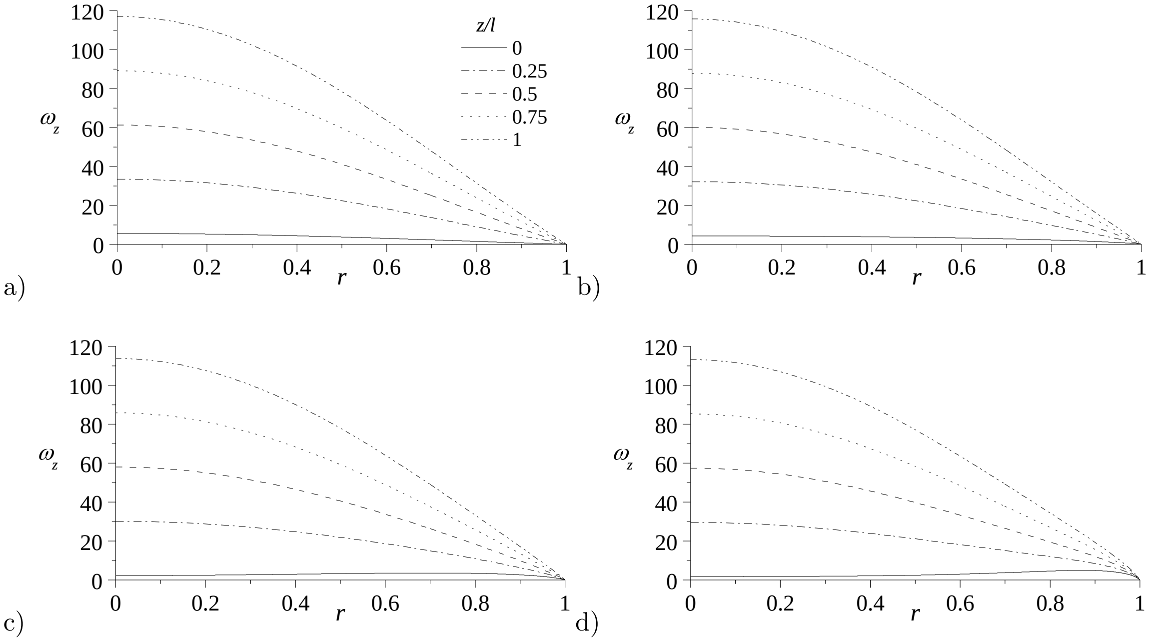

Figure 2.5. Analytical predictions of the axial vorticity distribution at five axial stations corresponding to a) self similar, b) Poiseuille, c) pseudo cosine, and d) power law injection patterns at entry.

then deviate both in the radial and streamwise directions. Radially, the Trkalian ω_θ reaches its peak value a short distance above the sidewall, as the flow progresses downstream, except for the power law model. In contrast, the maximum TC vorticity is always realized at the sidewall. Although both TC and Trkalian vorticities vanish at the centerline, the amount of TC vorticity remains almost insignificant in the core region for approximately a quarter diameter, and then climbs at a high radial rate to the point of always exceeding its Trkalian counterpart at the sidewall. Conversely, the Trkalian ω_θ begins to increase at a higher initial rate near the centerline, and then more gradually approaches its terminal value at the sidewall.

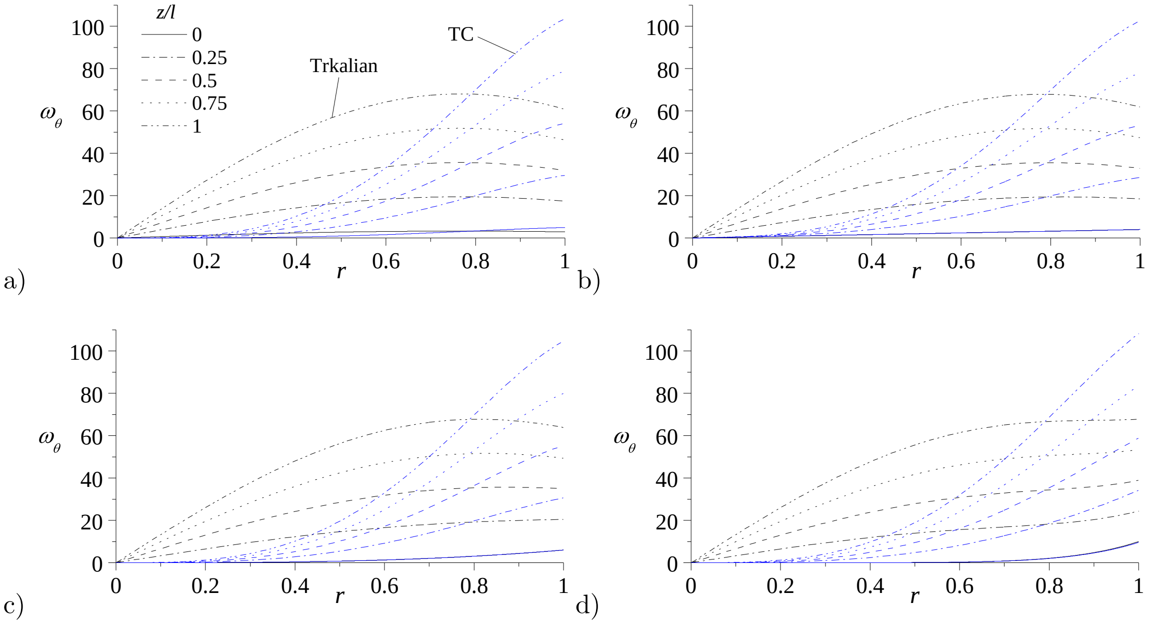

Figure 2.6. Analytical predictions of the tangential vorticity distribution at five axial stations corresponding to a) self similar, b) Poiseuille, c) pseudo cosine, and d) power law injection patterns at entry. Results are shown for both Trkalian and extended Taylor-Culick models [23].

To further illustrate the connection between $\boldsymbol{\omega}$ and ψ in the four representative injection cases, streamlines marked with arrowheads are overlaid in Fig. 2.7 on top of vorticity isocontours based on their total modulus, $\sqrt{{\omega_r}^2 + {\omega_\theta}^2 + {\omega_z}^2}$. Forthwith, one may note the more abrupt turning of the incoming streamlines as the radial gradient of the axial velocity near the sidewall, $\partial u_z(1, z)/\partial r$, becomes incrementally larger with the successive flattening of the inlet profiles. Note that a visible disparity in vorticity contours may be observed between the Poiseuille and pseudo cosine cases especially that ω_θ in the pseudo cosine formulation becomes negligible over the central portion of the chamber. In keeping with previous observations, both the streamline and vorticity contours begin with noticeable departures in the headwall region, and

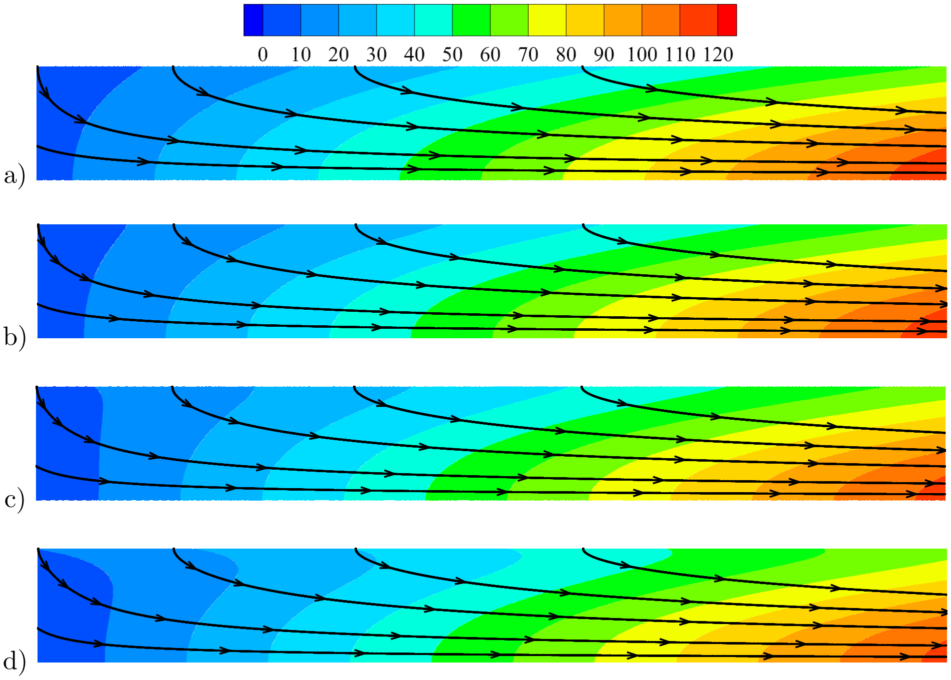

Figure 2.7. Trkalian streamlines and vorticity contours for a) self similar, b) Poiseuille, c) pseudo cosine, and d) power law injection patterns.

then spatially evolve to match the self similar solution in the downstream sections of the chamber.

For the purpose of comparison, TC streamlines and vorticity isocontours are showcased in Fig. 2.8 using the same four headwall injection patterns. In relation to Fig. 2.7, the TC streamlines exhibit a tighter turning radius as they convect away from the sidewall as previously reported by Majdalani and Fist [29]. As one would expect, the slow growth of ω_θ around the centerline is mirrored in its TC isovorticity contours where much of the core region remains nearly irrotational. Moreover, the spatial shifts in vorticity distributions as the inlet profiles become blunter is less

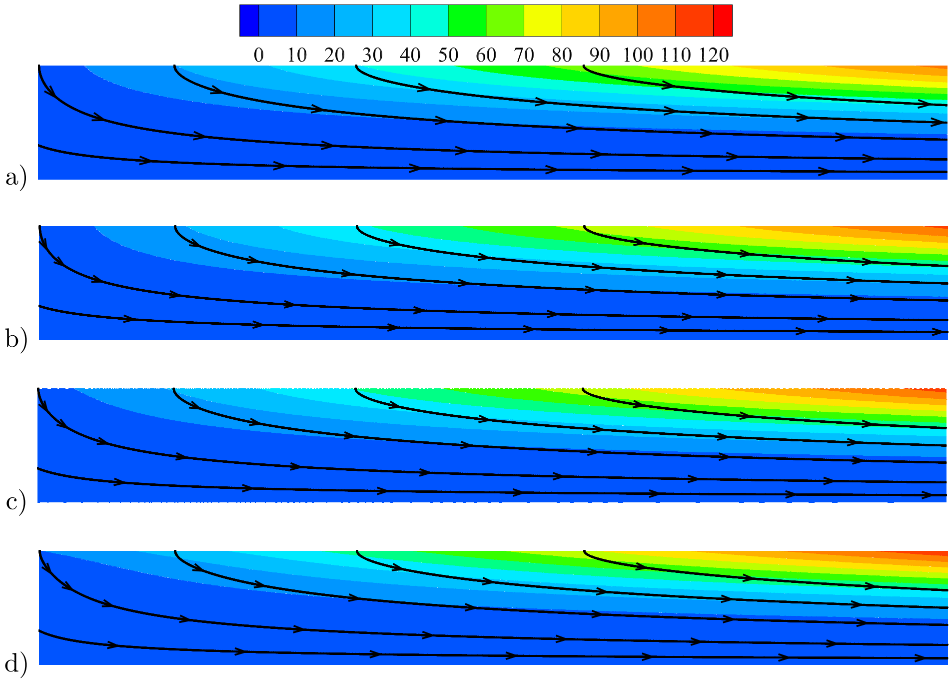

Figure 2.8. Taylor-Culick streamlines and vorticity contours for a) self similar, b) Poiseuille, c) pseudo cosine, and d) power law injection patterns.

substantial in the TC case where the overall shape remains nearly invariant despite the slight ω_θ increase that is witnessed near the sidewall.

2.2.4 Residual Error

As alluded to earlier, summing over $c_0 = \lambda_n$ leads to a small error in the final results due to c_0 being single valued in the original Bragg-Hawthorne formulation [23]. The residual $Q(r, z)$ may be determined by examining the vorticity transport equation (VTE) given by

$$\nabla \times (\boldsymbol{u} \times \boldsymbol{\omega}) = 0 \tag{2.34}$$

Upon expanding Eq. (2.34) under axisymmetric conditions, one recovers

$$-\frac{\partial}{\partial z}\left(u_z\omega_r - u_r\omega_z\right)\hat{\boldsymbol{e}}_r + \left[\frac{\partial}{\partial z}\left(u_\theta\omega_z - u_z\omega_\theta\right) - \frac{\partial}{\partial r}\left(u_r\omega_\theta - u_\theta\omega_r\right)\right]\hat{\boldsymbol{e}}_\theta + \frac{1}{r}\left\{\frac{\partial}{\partial r}\left[r\left(u_z\omega_r - u_r\omega_z\right)\right]\right\}\hat{\boldsymbol{e}}_z = 0 \quad (2.35)$$

In order for Eq. (2.35) to be satisfied, each component must vanish independently; however, when considering nonlinear coupling between eigenmodes, this will not be the case in general. To quantify the resulting error, it is useful to define a residual Q for each component of the vorticity transport equation using the standard nomenclature:

$$Q_r = -\frac{\partial}{\partial z}\left(u_z\omega_r - u_r\omega_z\right) \quad (2.36)$$

$$Q_\theta = \frac{\partial}{\partial z}\left(u_\theta\omega_z - u_z\omega_\theta\right) - \frac{\partial}{\partial r}\left(u_r\omega_\theta - u_\theta\omega_r\right) \quad (2.37)$$

$$Q_z = \frac{1}{r}\left\{\frac{\partial}{\partial r}\left[r\left(u_z\omega_r - u_r\omega_z\right)\right]\right\} \quad (2.38)$$

Upon substitution of the velocity, Eqs. (2.20–2.22), and vorticity, Eq. (2.33), expressions, we find that the radial component of the residual vanishes identically. This is quite understandable when taking into account that the derivative with respect to z removes any dependence on the summation terms, namely, those that are responsible for introducing the error, along with the fact that u_r and ω_r remain completely independent of z. These simplifications, however, do not convey to Q_θ and Q_z as radial derivatives appear in their expressions. In fact, after some algebra, Q_θ and Q_z

may be written as

$$\begin{aligned} Q_\theta = \frac{2J_1(\lambda_1 r)}{J_1(\lambda_1)} \Bigg\{ & \sum_{n=2}^{\infty} \frac{\lambda_n^2 \mathcal{I}_{h,n} J_0(\lambda_n r)}{J_1^2(\lambda_n)} - \lambda_1^2 \sum_{n=2}^{\infty} \frac{\mathcal{I}_{h,n} J_0(\lambda_n r)}{J_1^2(\lambda_n)} \\ & + \frac{2}{r} \left[\lambda_1 \sum_{n=2}^{\infty} \frac{\mathcal{I}_{h,n} J_1(\lambda_n r)}{J_1^2(\lambda_n)} - \sum_{n=2}^{\infty} \frac{\lambda_n \mathcal{I}_{h,n} J_1(\lambda_n r)}{J_1^2(\lambda_n)} \right] \Bigg\} \end{aligned} \tag{2.39}$$

$$\begin{aligned} Q_z = \frac{2}{J_1(\lambda_1)} \Bigg[& \lambda_1 J_1(\lambda_1 r) \sum_{n=2}^{\infty} \frac{\lambda_n \mathcal{I}_{h,n} J_1(\lambda_n r)}{J_1^2(\lambda_n)} - J_1(\lambda_1 r) \sum_{n=2}^{\infty} \frac{\lambda_n^2 \mathcal{I}_{h,n} J_1(\lambda_n r)}{J_1^2(\lambda_n)} \\ & + \lambda_1 J_0(\lambda_1 r) \sum_{n=2}^{\infty} \frac{\lambda_n \mathcal{I}_{h,n} J_0(\lambda_n r)}{J_1^2(\lambda_n)} - \lambda_1^2 J_0(\lambda_1 r) \sum_{n=2}^{\infty} \frac{\mathcal{I}_{h,n} J_0(\lambda_n r)}{J_1^2(\lambda_n)} \Bigg] \end{aligned} \tag{2.40}$$

Here it should be noted that each of the series contained in Eqs. (2.39–2.40) converges for the injection profiles of interest on the interval $r \in [0, 1]$ (see Appendix for series convergence detail), except for the second series in Eq. (2.40), which diverges at the sidewall as $r \to 1$. This outcome may be attributed to the inviscid nature of the present analysis, which is incapable of securing the no slip condition at the sidewall. A viscous correction to the tangential velocity will hence be necessary as will be demonstrated in the next section. In addition, careful consideration of the residual reveals that the error will be strongly affected by the difference between the single eigenvalue case (i.e., λ_1) and the summation over the totality of eigenvalues needed to capture an arbitrary headwall injection profile. In this context, it may be worthwhile noting that Q_θ appears at first glance to contain a singularity at $r = 0$; however, when the r^{-1} term is distributed within the series, the limit as $r \to 0$ produces

$$\lim_{r \to 0} \frac{J_1(\lambda_n r)}{r} = \frac{\lambda_n}{2} \tag{2.41}$$

When multiplied by another first order Bessel function of the first kind, the singular Q_θ term vanishes at $r = 0$. As for the corresponding centerline value of Q_z, it may be extracted from Eq. (2.40) and rearranged into

$$Q_z|_{r=0} = \frac{2\lambda_1}{J_1(\lambda_1)} \sum_{n=2}^{\infty} \frac{\mathcal{I}_{h,n}}{J_1^2(\lambda_n)} (\lambda_n - \lambda_1) \tag{2.42}$$

which remains independent of z. This ensures that the relative size of the residual will continually diminish with increasing distance from the headwall.

2.3 Viscous Wall Correction

2.3.1 Viscous Formulation

As alluded to in Sec. 2.2.4, one series summation in the inviscid Q_z fails to converge at the sidewall. The divergent term stems from the radial derivative of ω_z, which is overruled by the tangential velocity and its variation rate with respect to r, as per Eq. (2.32). To overcome this deficiency and permit u_θ to vanish at the sidewall, we turn our attention to the method of matched asymptotic expansions, which allows us to retrieve a viscous correction near the sidewall. The procedure presented here closely follows that of Majdalani and Fist [29].

We begin with the radial and tangential components of the normalized Navier-Stokes equations, specifically,

$$\begin{aligned}\frac{\partial p}{\partial r} = \frac{1}{Re}\left(\frac{\partial^2 u_r}{\partial r^2} + \frac{1}{r}\frac{\partial u_r}{\partial r} + \frac{1}{r^2}\frac{\partial^2 u_r}{\partial \theta^2} + \frac{\partial^2 u_r}{\partial z^2} - \frac{u_r}{r^2} - \frac{2}{r^2}\frac{\partial u_\theta}{\partial \theta}\right)& \\ - u_r\frac{\partial u_r}{\partial r} - \frac{u_\theta}{r}\frac{\partial u_r}{\partial \theta} - u_z\frac{\partial u_r}{\partial z} + \frac{u_\theta^2}{r}& \qquad (2.43)\\ \frac{\partial p}{\partial \theta} = r\frac{1}{Re}\left(\frac{\partial^2 u_\theta}{\partial r^2} + \frac{1}{r}\frac{\partial u_\theta}{\partial r} + \frac{1}{r^2}\frac{\partial^2 u_\theta}{\partial \theta^2} + \frac{\partial^2 u_\theta}{\partial z^2} - \frac{u_\theta}{r^2} - \frac{2}{r^2}\frac{\partial u_r}{\partial \theta}\right)& \\ - r\left(u_r\frac{\partial u_\theta}{\partial r} - \frac{u_\theta}{r}\frac{\partial u_\theta}{\partial \theta} - u_z\frac{\partial u_\theta}{\partial z} + \frac{u_r u_\theta}{r}\right)& \qquad (2.44)\end{aligned}$$

where $1/Re = \nu/(U_w a) = \epsilon$. By sequentially taking the tangential derivative of Eq. (2.43), the radial derivative of Eq. (2.44), equating the mixed derivatives of the pressure, and making use of axisymmetry, we arrive at

$$\frac{\partial}{\partial r}\left[\epsilon r\left(\frac{\partial^2 u_\theta}{\partial r^2} + \frac{1}{r}\frac{\partial u_\theta}{\partial r} + \frac{\partial^2 u_\theta}{\partial z^2} - \frac{u_\theta}{r^2}\right) - r\left(u_r\frac{\partial u_\theta}{\partial r} + u_z\frac{\partial u_\theta}{\partial z} + \frac{u_r u_\theta}{r}\right)\right] = 0 \qquad (2.45)$$

At this point, we substitute $u_\theta = zf(r) + F(r)$ and $u_z = zg(r) + G(r)$ into Eq. (2.45) to obtain

$$\begin{aligned} z\Bigg\{\epsilon\left(rf''' + 2f'' - \frac{1}{r}f' + \frac{1}{r^2}f\right)& \\ - \left[2u_r f' + gf + u_r' f + r\left(u_r' f' + u_r f'' + g' f + g f'\right)\right]\Bigg\}& \\ + \epsilon\left(rF''' + 2F'' - \frac{1}{r}F' + \frac{1}{r^2}F\right)& \\ - \left[2u_r F' + Gf + u_r' F + r\left(u_r' F' + u_r F'' + G' f + G f'\right)\right] = 0& \qquad (2.46)\end{aligned}$$

Realizing that $u_r' = -g(r) - u_r/r$ and neglecting terms that stem from the axial velocity near the sidewall (where u_z vanishes), we are left with

$$z\left[\epsilon\left(rf''' + 2f'' - \frac{1}{r}f' + \frac{1}{r^2}f\right) - u_r\left(-rf'' - f' + \frac{1}{r}f\right)\right] \\ + \epsilon\left(rF''' + 2F'' - \frac{1}{r}F' + \frac{1}{r^2}F\right) - u_r\left(-rF'' - F' + \frac{1}{r}F\right) = 0 \quad (2.47)$$

We hence identify two equations of identical form that must vanish in parallel in order to secure Eq. (2.46). We focus on the coefficient of z and realize that the resulting expression for the coefficient of z^0 is identical. To make further headway, we recognize that $B_z = rf$ must be the form of the tangential angular momentum that increases linearly in z. After some rearrangements, we get

$$\epsilon\left(B_z''' - \frac{1}{r}B'' + \frac{1}{r^2}B_z'\right) - u_r\left(B_z'' - \frac{1}{r}B_z'\right) = 0 \quad (2.48)$$

2.3.2 Asymptotic Solution

In the interest of capturing the sidewall boundary layer, the independent variable may be stretched according to the wall coordinate transformation, $r_w = (1 - r)/\delta_w$. Upon substitution and order of magnitude segregation to eliminate unessential quantities, Eq. (2.48) becomes

$$\frac{\epsilon}{\delta_w^3}\left[\dddot{B}_z^{(w)} + \delta_w \ddot{B}_z^{(w)} + \delta_w^2 \dot{B}_z^{(w)}\right] - \frac{1}{\delta_w^2}\left[u_r^{(0)} \ddot{B}_z{}^{(w)} + \delta_w u_r'^{(0)} \dot{B}_z^{(w)}\right] = 0 \quad (2.49)$$

where the superscripts '(w)' and '(0)' refer to either a wall-based or an outer, farfield expansion. Since the boundary layer is 'blown off' the sidewall due to inward gaseous injection, it is important to properly model the area that hangs between the outer, farfield region, where the inward, radial mass flux dominates, and the core region, where the axial velocity overtakes the motion. As originally determined by Cole and Aroesty [36], the unlocalized layer where viscous forces become significant occurs where $u_r\ddot{B}_z(w)$ ceases to matter. This term stems from $u_r(\partial u_\theta)/(\partial r)$ in the θ-component of the Navier-Stokes equations, which represents the radial component of the convective derivative of u_θ. When this assumption is integrated, it may be straightforwardly shown that a distinguished limit of $\delta_w \sim \epsilon^{1/2}$ will induce a balance between the viscous term and the remaining inertial term in Eq. (2.49). At leading order, we extract

$$\dddot{B}_z^{(w)} - \dot{B}_z^{(w)} = 0 \tag{2.50}$$

where $u_r'^{(0)} \approx 1$ near the wall.

The boundary conditions placed on Eq. (2.50) consist of the velocity adherence requirement at the sidewall and the seamless merging with the outer, inviscid flowfield away from the wall. Algebraically, these translate into

$$B_z^{(w)}|_{r_w=0} = 0 \tag{2.51}$$

$$\lim_{r_w\to\infty} B_z^{(w)} = r_0 f(r_0) = r_0\lambda_1 \frac{J_1(\lambda_1 r_0)}{J_1(\lambda_1)} \tag{2.52}$$

where $r_0 = r$ denotes the unstretched radial coordinate. At this juncture, direct integration of Eq. (2.50) yields

$$B_z^{(w)} = b_0 + b_1 e^{-r_w} + b_2 e^{r_w} \tag{2.53}$$

which must be solved for the three unknowns, (b_0, b_1, b_2). Firstly, by virtue of Eq. (2.52), preventing unboundedness as $r_w \to \infty$ requires setting $b_2 = 0$. Secondly, application of Eq. (2.51) renders $b_0 = -b_1$. Thirdly, matching with the outer solution leaves us with

$$B_z^{(w)} = rf^{(w)} = [1 - e^{-(1-r)\sqrt{Re}}]r\lambda_1 \frac{J_1(\lambda_1 r)}{J_1(\lambda_1)} \tag{2.54}$$

where r_0 and r_w have been converted back to their unstretched coordinate representations. Similarly for the z^0 term of Eq. (2.47), we recover

$$rF^{(w)} = [1 - e^{-(1-r)\sqrt{Re}}]r \sum_{n=1}^{\infty} \frac{2\lambda_n \mathcal{I}_{h,n} J_1(\lambda_n r)}{J_1^2(\lambda_n)} \tag{2.55}$$

The wall-rectified tangential velocity may hence be achieved by consolidating Eqs. (2.54–2.55) into

$$\begin{aligned} u_\theta^{(w)} &\approx zf^{(w)} + F^{(w)} \\ &\approx \left[1 - e^{-(1-r)\sqrt{Re}}\right] \left\{ \left[\lambda_1 z + \frac{2\mathcal{I}_{h,1}}{J_1(\lambda_1)}\right] \frac{J_1(\lambda_1 r)}{J_1(\lambda_1)} + \sum_{n=2}^{\infty} \frac{2\mathcal{I}_{h,n} J_1(\lambda_n r)}{J_1^2(\lambda_n)} \right\} \end{aligned} \tag{2.56}$$

The ability of Eq. (2.56) to satisfy the velocity adherence requirement at the sidewall is illustrated in Fig. 2.9 at five axial stations and two Reynolds numbers of 100 and 1000 using the two bounding inlet profiles, namely, the self similar in Figs. 2.9a–2.9b and power law function in Figs. 2.9c–2.9d. Compared to the strictly inviscid approximation, the presence of a stationary sidewall is now felt within a boundary layer that is consistent with $\delta_w = 4.60517/\sqrt{Re}$ as previously shown by Majdalani and Fist [29]. As the Reynolds number is increased by one order of magnitude, the thinning of the wall boundary layer may be observed along with the radially outward bulging of the maximum swirl velocity region.

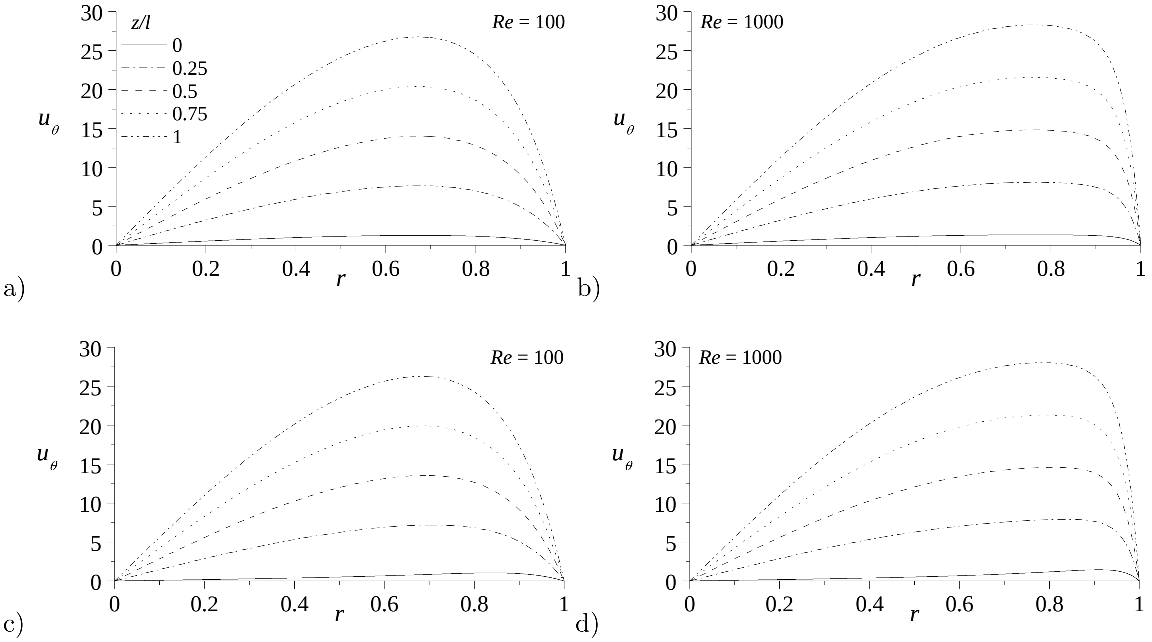

Figure 2.9. Analytical predictions of the rectified tangential velocity at five axial stations corresponding to (a-b) self similar and (c-d) power law injection profiles using two Reynolds numbers of 100 (left) and 1000 (right).

Before leaving this section, it may be instructive to note that a core boundary layer may be similarly pursued in the core region as $r \to 0$. However, the correction realized from the attendant analysis proves rather immaterial to the present formulation since u_θ already vanishes at the centerline to the extent that the role of the viscous core correction will be mainly to suppress the radial gradient of the tangential velocity as the flow approaches the chamber axis. Moreover, its connection with the headwall injection patterns may be viewed as inconsequential being axially independent and, therefore, insensitive to the user-specified $u_0(r)$ imposed at entry.

2.3.3 Rectified Vorticity and Residual

With the rectified tangential velocity in hand, the vorticity and residuals may be revisited. From Eq. (2.32), the vorticity components become

$$\tilde{\omega}_r = -\left[1 - e^{-(1-r)\sqrt{Re}}\right] \frac{\lambda_1 J_1(\lambda_1 r)}{J_1(\lambda_1)} \tag{2.57}$$

$$\tilde{\omega}_\theta = \left[\lambda_1 z + \frac{2\mathcal{I}_{h,1}}{J_1(\lambda_1)}\right] \frac{\lambda_1 J_1(\lambda_1 r)}{J_1(\lambda_1)} + \sum_{n=2}^{\infty} \frac{2\lambda_n \mathcal{I}_{h,n} J_1(\lambda_n r)}{J_1^2(\lambda_n)} \tag{2.58}$$

$$\begin{aligned}\tilde{\omega}_z = {} & \left[1 - e^{-(1-r)\sqrt{Re}}\right] \left\{ \left[\lambda_1 z + \frac{2\mathcal{I}_{h,1}}{J_1(\lambda_1)}\right] \frac{\lambda_1 J_0(\lambda_1 r)}{J_1(\lambda_1)} \right. \\ & \left. + \sum_{n=2}^{\infty} \frac{2\lambda_n \mathcal{I}_{h,n} J_0(\lambda_n r)}{J_1^2(\lambda_n)} \right\} - \sqrt{Re}\; e^{-(1-r)\sqrt{\Re}} \left\{ \left[\lambda_1 z + \frac{2\mathcal{I}_{h,1}}{J_1(\lambda_1)}\right] \frac{J_1(\lambda_1 r)}{J_1(\lambda_1)} \right. \\ & \left. + \sum_{n=2}^{\infty} \frac{2\mathcal{I}_{h,n} J_1(\lambda_n r)}{J_1^2(\lambda_n)} \right\}\end{aligned} \tag{2.59}$$

Substituting these expressions along with the rectified tangential velocity back into Eqs. (2.36–2.38) enables us to deduce the residual of the vorticity transport equation due to nonlinear coupling between eigenmodes as well as the viscous correction at the sidewall. Recalling that the inviscid form of the radial component of the residual is null, its presently finite value is solely prescribed by the viscous correction. It may be estimated from

$$\tilde{Q}_r = \left[1 - e^{-(1-r)\sqrt{Re}}\right] \frac{\lambda_1^2 J_1(\lambda_1 r)}{J_1^2(\lambda_1)} \left[J_1(\lambda_1 r) - J_0(\lambda_1 r)\right] + \sqrt{Re}\; e^{-(1-r)\sqrt{Re}} \frac{\lambda_1 J_1^2(\lambda_1 r)}{J_1^2(\lambda_1)} \tag{2.60}$$

In the above, $\tilde{Q}_r$ vanishes at the centerline and peaks near the sidewall where viscous effects become relevant. Furthermore, being independent of z, the residual error in the radial direction remains constant along the length of the chamber. This behavior is contrary to that of its tangential counterpart, specifically,

$$\begin{aligned}\tilde{Q}_\theta = \left[1 - e^{-(1-r)\sqrt{Re}}\right] \frac{2\lambda_1 J_1(\lambda_1 r)}{r J_1(\lambda_1)} &\left\{\left[\lambda_1 z + \frac{2\mathcal{I}_{h,1}}{J_1(\lambda_1)}\right] \frac{J_1(\lambda_1 r)}{J_1(\lambda_1)} + \sum_{n=2}^{\infty} \frac{2\mathcal{I}_{h,n} J_1(\lambda_n r)}{J_1^2(\lambda_n)}\right\} \\ &- \frac{2}{r}\left[\lambda_1 z + \frac{2\mathcal{I}_{h,1}}{J_1^2(\lambda_1)}\right] \frac{\lambda_1 J_1^2(\lambda_1 r)}{J_1^2(\lambda_1)} - \frac{J_1(\lambda_1 r)}{r J_1(\lambda_1)} \sum_{n=2}^{\infty} \frac{2\lambda_n \mathcal{I}_{h,n} J_1(\lambda_n r)}{J_1^2(\lambda_n)} \\ + \frac{J_1(\lambda_1 r)}{J_1(\lambda_1)} &\left\{\sum_{n=2}^{\infty} \frac{2\lambda_n \mathcal{I}_{h,n}}{J_1^2(\lambda_n)}\left[\lambda_n J_0(\lambda_n r) - \frac{1}{r} J_1(\lambda_n r)\right] - \lambda_1^2 \sum_{n=2}^{\infty} \frac{2\mathcal{I}_{h,n} J_0(\lambda_n r)}{J_1^2(\lambda_n)}\right\}\end{aligned} \tag{2.61}$$

Here a dependency on z appears due to the viscous correction. Nonetheless, the θ-component of the residual again vanishes at the centerline and condenses itself at the sidewall where

$$\tilde{Q}_\theta|_{r=1} = -2\left\{\lambda_1\left[\lambda_1 z + \frac{2\mathcal{I}_{h,1}}{J_1^2(\lambda_1)}\right] + \sum_{n=2}^{\infty} \frac{2\lambda_n \mathcal{I}_{h,n}}{J_1(\lambda_1)}\right\} \tag{2.62}$$

Along similar lines, the z-component of the residual may be computed from

$$\begin{aligned}
\tilde{Q}_z = \left[1 - e^{-(1-r)\sqrt{Re}}\right] & \left\{ \frac{J_1(\lambda_1 r)}{J_1(\lambda_1)} \left[\lambda_1 \sum_{n=2}^{\infty} \frac{2\lambda_n \mathcal{I}_{h,n} J_1(\lambda_n r)}{J_1^2(\lambda_n)} - \sum_{n=2}^{\infty} \frac{2\lambda_n^2 \mathcal{I}_{h,n} J_1(\lambda_n r)}{J_1^2(\lambda_n)} \right] \right. \\
& \left. + \frac{\lambda_1 J_0(\lambda_1 r)}{J_1(\lambda_1)} \sum_{n=2}^{\infty} \frac{2\mathcal{I}_{h,n} J_0(\lambda_n r)}{J_1^2(\lambda_n)} (\lambda_n - \lambda_1) \right\} \\
+ \sqrt{Re}\; e^{-(1-r)\sqrt{Re}} & \left\{ \frac{J_1(\lambda_1 r)}{J_1^2(\lambda_1)} \left[\lambda_1 z + \frac{2\mathcal{I}_{h,1}}{J_1(\lambda_1)} \right] \left[\frac{1}{r} J_1(\lambda_1 r) - 2\lambda_1 J_0(\lambda_1 r) \right] \right. \\
& + \frac{\lambda_1}{J_1(\lambda_1)} \sum_{n=2}^{\infty} \frac{2\mathcal{I}_{h,n}}{J_1^2(\lambda_n)} \left[J_1(\lambda_1 r) J_0(\lambda_n r) - J_0(\lambda_1 r) J_1(\lambda_n r) \right] \\
& \left. + \frac{J_1(\lambda_1 r)}{J_1(\lambda_1)} \sum_{n=2}^{\infty} \frac{2\mathcal{I}_{h,n}}{J_1^2(\lambda_n)} \left[\frac{1}{r} J_1(\lambda_n r) - 2\lambda_n J_0(\lambda_n r) \right] \right\} \\
- Re\; e^{-(1-r)\sqrt{Re}}\; \frac{J_1(\lambda_1 r)}{J_1(\lambda_1)} & \left\{ \left[\lambda_1 z + \frac{2\mathcal{I}_{h,1}}{J_1(\lambda_1)} \right] \frac{J_1(\lambda_1 r)}{J_1(\lambda_1)} + \sum_{n=2}^{\infty} \frac{2\mathcal{I}_{h,n} J_1(\lambda_n r)}{J_1^2(\lambda_n)} \right\} \qquad (2.63)
\end{aligned}$$

Despite its generally formidable character, $\tilde{Q}_z$ reduces at the centerline into a one term summation,

$$\begin{aligned}
\tilde{Q}_z|_{r=0} &= \left(1 - e^{-\sqrt{Re}}\right) \frac{2\lambda_1}{J_1(\lambda_1)} \sum_{n=2}^{\infty} \frac{\mathcal{I}_{h,n}}{J_1^2(\lambda_n)} (\lambda_n - \lambda_1) \\
&\approx \frac{2\lambda_1}{J_1(\lambda_1)} \sum_{n=2}^{\infty} \frac{\mathcal{I}_{h,n}}{J_1^2(\lambda_n)} (\lambda_n - \lambda_1)
\end{aligned} \qquad (2.64)$$

Although the foregoing expression resembles its inviscid form, it has the added advantage of remaining bounded at the sidewall as a result of the vanishing of its ill-behaving series, which is now multiplied by $\{1 - \exp[-(1-r)\sqrt{Re}]\} \to 0$ as $r \to 1$.

2.4 Conclusions

In this chapter, a generalization of the swirling Trkalian model developed by Majdalani and Fist [29] is extended in the context of a right-cylindrical porous chamber with arbitrary headwall injection patterns. The resulting description may be used as a bulk flow idealization for modeling HREs with an oxidizer injector faceplate or SRMs with an end-burning grain at their fore-end closure. An interesting feature of the Trkalian model lies in its ability to exhibit a swirling velocity component that stands to enhance the regression rate of both SRM and HRE grains. Beginning with the Bragg-Hawthorne equation, we show that when both superposition and orthogonality principles are applied in unison, it is possible to capture the effects of an arbitrarily prescribed injection profile at the chamber's fore end. This feature is illustrated using four explicitly defined inlet test cases that correspond to self similar, Poiseuille, pseudo cosine, and power law profiles. For each of the inlet models under consideration, the evolution of the fundamental flowfield variables is described throughout the chamber. By way of verification, the problem is numerically simulated using a finite volume solver and a carefully developed structured grid. Simulation results are then compared to the analytical predictions for each of the inlet profiles and shown to agree quite favorably in all three spatial directions. In this vein, our analysis suggests that, as the distance from the headwall is increased, a steady convergence to the similarity-conforming solution will occur, consistently with the findings of Kurdyumov [35] and Majdalani and Saad [23]. The observed behavior is further confirmed from the vorticity formulation and its isocontours, which clearly show that the exact Trkalian nature of the flowfield will be restored as $z \to \infty$.

As for the residual error caused by the nonlinear coupling between eigenmodes, it also leads to a form that is independent of z, thus furthering our confidence in the approximate solutions as the flow evolves downstream. After detecting a singularity in the z-component of the residual, where a single series fails to converge, a viscous correction to the tangential velocity near the sidewall is pursued using boundary layer theory and the tools of matched asymptotic expansions. Unsurprisingly, the incorporation of small viscosity is proven to rectify this deficiency. The resulting expression for $u_\theta^{(w)}$ is shown to vanish as $r \to 1$ in fulfillment of the no slip requirement. After revisiting the residual, we are able to confirm that the rectified $\tilde{Q}_z$ remains bounded at the sidewall while retaining its inviscid character in the core region.

Overall, despite the inherent error in our series approximations, numerical verifications along with the streamwise convergence of our formulation onto the exact solution after some distance from the headwall lend confidence to our model's ability to faithfully reproduce the effects of arbitrary headwall injection. In future investigations, we hope to employ the present framework to improve regression rate models of SRMs and HREs by accounting for both swirl and problem-specific headwall injection patterns.

Chapter 3

Compressible Trkalian Profile

In this Chapter, we return to the exact self-similar solution, which constitutes the foundational mean flowfield to which compressible corrections may be appended. The approach that we follow will be initiated from the coupled compressible Bragg-Hawthorne equation and density relations, using a Rayleigh-Janzen expansion in the wall Mach number squared. After some effort, a compressible swirling motion will be constructed, characterized, and compared to its Taylor-Culick analog.

3.1 Compressible Bragg-Hawthorne Framework

Beginning with the normalized variables of Sec. 1.2.2, we may express the fundamental equations of motion that stand at the foundation of the compressible Bragg-Hawthorne equation, namely,

$$\nabla \cdot (\rho \boldsymbol{u}) = 0 \qquad \text{(conservation of mass)} \tag{3.1}$$

$$\nabla \cdot (\rho H \boldsymbol{u}) = 0 \qquad \text{(conservation of energy)} \tag{3.2}$$

$$\boldsymbol{u} \cdot \boldsymbol{u} = -\frac{\nabla p}{\gamma M_w^2 \rho} \qquad \text{(conservation of momentum)} \tag{3.3}$$

$$H = \frac{1}{2}\boldsymbol{u} \cdot \boldsymbol{u} + \frac{1}{(\gamma - 1) M_w^2}\frac{p}{\rho} \qquad \text{(stagnation head)} \tag{3.4}$$

Now, a brief overview of the compressible Bragg-Hawthorne framework as developed by Maicke and Majdalani [30] is presented. Fundamental to the Bragg-Hawthorne equation is the recognition that the stagnation head, as well as the tangential angular momentum are expressible in terms of the stream function alone. From the above fundamental equations it can be shown that, under the assumptions of axisymmetric and isentropic flow, the gradient of H does not return a component in the direction of the velocity field, or $\nabla H \cdot \boldsymbol{u} = 0$. By remaining constant along streamlines, it leads to the conclusion that the stagnation head must be a function of the stream function alone. In the same vein, it can be shown that the tangential angular momentum B must be a function of the stream function only, specifically,

$$H = H(\psi) \qquad \text{and} \qquad B = B(\psi) \tag{3.5}$$

With the two above relations and the conditions of steady, isentropic, axisymmetric flow, the compressible Bragg-Hawthorne equation collapses into

$$\mathrm{D}^2\psi + \rho^2\left(B\frac{\mathrm{d}B}{\mathrm{d}\psi} - r^2\frac{\mathrm{d}H}{\mathrm{d}\psi}\right) = \frac{1}{\rho}\nabla\rho\cdot\nabla\psi; \quad \mathrm{D}^2 \equiv \frac{\partial^2}{\partial r^2} - \frac{1}{r}\frac{\partial}{\partial r} + \frac{\partial^2}{\partial z^2} \tag{3.6}$$

where D^2 symbolizes the axisymmetric Stokes operator. However, one additional equation is still needed to achieve closure. This can be accomplished by invoking the isentropic relations and replacing the velocities in the stagnation head by the stream function, and the pressure by the density. We hence arrive at

$$H - \frac{B^2}{2r^2} = \frac{1}{2\rho^2 r^2}\left[\left(\frac{\partial\psi}{\partial z}\right)^2 + \left(\frac{\partial\psi}{\partial r}\right)^2\right] + \frac{\rho^{\gamma-1}}{(\gamma-1)\,M_w^2} \tag{3.7}$$

With the two equations of interest in hand, suitable choices for H and B along with a Rayleigh-Janzen expansion may be pursued to produce a set of equations that may be solved sequentially for the leading-order stream function as well as its higher order compressible corrections. Maicke and Majdalani [30] show that a suitable set of assumptions for H and B are

$$\begin{aligned} H &= \frac{1}{(\gamma-1)\,M_w^2}; \quad \frac{\mathrm{d}H}{\mathrm{d}\psi} = 0 \\ B &= \sqrt{c_0^2\psi^2 + c_1^2 + M_w^2\psi^2\left(c_2^2 + \tfrac{1}{2}c_3^2\psi^2\right)} \\ B\frac{\mathrm{d}B}{\mathrm{d}\psi} &= c_0^2\psi + M_w^2\psi\left(c_2^2 + c_3^2\psi^2\right) \end{aligned} \tag{3.8}$$

Using a conventional Rayleigh-Janzen expansion and expanding the variables of interest in terms of M_w^2, the following Bragg-Hawthorne terms may be segregated at leading and first order:

$$O(1){:}\quad \mathrm{D}^2\psi_0 + c_0^2\psi_0 = 0 \tag{3.9}$$

$$O(M_w^2){:}\quad \mathrm{D}^2\psi_1 + c_0^2\psi_1 = \nabla\psi_0\cdot\nabla\rho_1 - 2\rho_1 c_0^2\psi_0 - c_2^2\psi_0 - c_3^2\psi_0^3 \tag{3.10}$$

The corresponding leading and first order density relations may be similarly extracted and expressed as

$$O(M_w^2){:}\quad \rho_1 = -\frac{1}{2r^2}\left[\left(\frac{\partial\psi_0}{\partial z}\right)^2 + \left(\frac{\partial\psi_0}{\partial r}\right)^2 + c_0^2\psi_0^2\right] \tag{3.11}$$

$$\begin{aligned} O(M_w^4){:}\quad \rho_2 = -\frac{2+\gamma}{2}\rho_1^2 - \frac{\rho_1}{r^2}\left[c_0^2\psi_0^2 + c_1^2\right] - \frac{\psi_0}{2r^2}\big[2c_0^2\psi_1 \\ + c_2^2\psi_0^2 + c_3^2\psi_0^3\big] - \frac{1}{r^2}\left[\frac{\partial\psi_0}{\partial z}\frac{\partial\psi_1}{\partial z} + \frac{\partial\psi_0}{\partial r}\frac{\partial\psi_1}{\partial r}\right] \end{aligned} \tag{3.12}$$

Equations (3.9–3.12) encapsulate the compressible Bragg-Hawthorne framework as set forth by Maicke and Majdalani [30]. Accordingly, Eq. (3.9) can be solved for ψ_0 and the result substituted into Eq. (3.11), thus providing the means to determine ρ_1. The outcome for ρ_1 may then be inserted into Eq. (3.10) to deduce ψ_1, hence arriving at the first order compressible correction; this process may be repeated until a desired level of accuracy is achieved.

3.2 Boundary Conditions

The boundary conditions imposed are identical to those in Sec. 1.2.3 with the exception of the Headwall injection profile. Here, the analysis is limited to the self-similarity case for which

$$u_z(r,0) = u_c J_0(\lambda_1 r) = u_h \lambda_1 J_0(\lambda_1 r)/J_1(\lambda_1) \tag{3.13}$$

When these conditions are conveyed to the compressible stream function, we are left with

$$-\frac{1}{\rho r}\frac{\partial \psi}{\partial z}\bigg|_{(0,z)} = 0 \qquad \text{(no radial flow across centerline)} \tag{3.14}$$

$$-\frac{1}{\rho r}\frac{\partial \psi}{\partial z}\bigg|_{(1,z)} = -1 \qquad \text{(radial velocity at the sidewall)} \tag{3.15}$$

$$\frac{1}{\rho r}\frac{\partial \psi}{\partial r}\bigg|_{(1,z)} = 0 \qquad \text{(no axial slip at the sidewall)} \tag{3.16}$$

$$\frac{1}{\rho r}\frac{\partial \psi}{\partial r}\bigg|_{(r,0)} = u_c J_0(\lambda_1 r) \qquad \text{(prescribed headwall injection)} \tag{3.17}$$

$$\frac{1}{r}B(\psi)\bigg|_{(0,0)} = 0 \qquad \text{(no swirl velocity at headwall center)} \tag{3.18}$$

Due to the expansion method used, care must be taken in the application of these boundary conditions. The same expansion must be employed to obtain conditions on the leading and first order terms. Whereas the leading order terms must capture the appropriate behavior at the boundaries, the corresponding first order terms must vanish in order to preserve the conditions already satisfied at leading order. Forthwith, the expansion of the first boundary condition leads to

$$u_r^{(0)} + M_w^2 u_r^{(1)} = -\frac{1}{r\left(1 + M_w^2 \rho_1\right)}\frac{\partial}{\partial z}\left(\psi_0 + M_w^2 \psi_1\right) \tag{3.19}$$

Subsequently, simplifying and equating like powers of M_w^2 yields the following expressions for the leading and first order radial velocities:

$$u_r^{(0)} = -\frac{1}{r}\frac{\partial \psi_0}{\partial z} \qquad u_r^{(1)} = \frac{\rho_1}{r}\frac{\partial \psi_0}{\partial z} - \frac{1}{r}\frac{\partial \psi_1}{\partial z} \tag{3.20}$$

Realizing that $u_r^{(0)}$ is present in the first member of $u_r^{(1)}$, the condition on the radial velocity, condition (a), at the centerline can be rewritten at leading and first orders as

$$-\frac{1}{r}\frac{\partial\psi_0}{\partial z}\bigg|_{(0,z)} = 0 \qquad\qquad -\frac{1}{r}\frac{\partial\psi_1}{\partial z}\bigg|_{(0,z)} = 0 \tag{3.21}$$

In like manner, the remaining boundary conditions may be expanded to produce, at leading and first order, the following assortment of coupled conditions:

$$-\frac{1}{r}\frac{\partial\psi_0}{\partial z}\bigg|_{(1,z)} = -1; \qquad \rho_1 - \frac{1}{r}\frac{\partial\psi_1}{\partial z}\bigg|_{(1,z)} = 0 \qquad \text{(b)} \tag{3.22}$$

$$\frac{1}{r}\frac{\partial\psi_0}{\partial r}\bigg|_{(1,z)} = 0; \qquad \frac{1}{r}\frac{\partial\psi_1}{\partial r}\bigg|_{(1,z)} = 0 \qquad \text{(c)} \tag{3.23}$$

$$\frac{1}{r}\frac{\partial\psi_0}{\partial r}\bigg|_{(r,0)} = u_c J_0(\lambda_1 r); \qquad \frac{1}{r}\frac{\partial\psi_1}{\partial r}\bigg|_{(r,0)} - \rho_1 u_c J_0(\lambda_1 r) = 0 \qquad \text{(d)} \tag{3.24}$$

$$\frac{1}{r}\sqrt{c_0^2\psi_0^2 + c_1^2}\bigg|_{(0,0)} = 0; \qquad \frac{c_0^2\psi_1\psi_0 + \frac{1}{2}c_2^2\psi_0^2 + \frac{1}{4}c_3^2\psi_0^4}{r\sqrt{c_0^2\psi_0^2 + c_1^2}}\Bigg|_{(0,0)} = 0 \qquad \text{(e)} \tag{3.25}$$

Before leaving this section, it may be instructive to note that the extraction of integration constants resulting from Eq. (3.24) may be simplified by evaluating the condition at the centerline. At leading order, it may be easily shown that the exact incompressible solution is readily recovered, for which condition (d) is met $\forall r$. At the first order, the compressible correction obtained using the Rayleigh-Janzen expansion will also satisfy condition (d), albeit asymptotically.

3.3 Leading Order Solution

By expanding the Stokes operator in Eq. (3.9), the incompressible Bragg-Hawthorne equation is immediately restored viz.

$$\frac{\partial^2 \psi_0}{\partial r^2} - \frac{1}{r}\frac{\partial \psi_0}{\partial r} + \frac{\partial \psi_0^2}{\partial z^2} + c_0^2 \psi_0 = 0 \tag{3.26}$$

Equation (3.26) is identical to Eq. (3.4) and leads to the type 0 solution given by

$$\psi_0(r,z) = r\,(k_1 z + k_2)\,[k_3 J_1(c_0 r) + k_4 Y_1(c_0 r)] \tag{3.27}$$

The boundary conditions may now be imposed on the leading order stream function as presented in Eqs. (3.21–3.25). To avoid singularities as $r \to 0$ in the process of satisfying condition (a) we take $k_4 = 0$. In like manner, enforcing axial no-slip, condition (c), requires c_0 to be one of the zeroes of the zeroth-order Bessel function of the first kind. Furthermore, to retain similarity with the comparable Trkalian profile [29], we pursue the partial solution corresponding to the first zero of the zeroth-order Bessel function of the first kind by taking $c_0 = \lambda_1 \approx 2.40483$. Subsequently, securing the uniform injection condition (b) at the sidewall results in $k_1 = 1/J_1(\lambda_1) \approx 1.92623$, whereas the prescribed headwall injection condition (d) returns $k_2 = u_h$. Finally, securing the tangential velocity requirement (e) leaves us with $c_1 = 0$. In view of these simplifications, the leading order stream function and its associated tangential velocity collapse into

$$\psi_0(r,z) = r(z+u_h)\frac{J_1(\lambda_1 r)}{J_1(\lambda_1)} \qquad u_\theta = (z+u_h)\frac{\lambda_1 J_1(\lambda_1 r)}{J_1(\lambda_1)} \tag{3.28}$$

As expected, the leading order asymptotic expansion reproduces the Trkalian, Majdalani-Fist profile [29]. Substituting the above expression into Eq. (3.11) enables us to retrieve the first density correction via

$$\rho_1 = -\frac{1}{2J_1^2(\lambda_1)}\left\{J_1^2(\lambda_1 r) + \lambda_1^2\left(z+u_h\right)^2\left[J_0^2(\lambda_1 r) + J_1^2(\lambda_1 r)\right]\right\} \tag{3.29}$$

3.4 First Order Solution

The first order Bragg-Hawthorne equation presents a more challenging problem due to the non-homogeneous terms that appear on its right hand side. Making appropriate substitutions into Eq. (3.10) and using the previous results for ψ_0 and ρ_1, we arrive at

$$\begin{aligned} \mathrm{D}^2\psi_1 + \lambda_1^2\psi_1 = \frac{r\left(z+u_h\right)J_1(\lambda_1 r)}{J_1^3(\lambda_1)} & \left\{\lambda_1^4\left(z+u_h\right)^2\left[J_0^2(\lambda_1 r) + J_1^2(\lambda_1 r)\right]\right. \\ & \left. -2\lambda_1^2 J_0^2(\lambda_1 r) - c_2^2 J_1^2(\lambda_1) - c_3^2 r^2\left(z+u_h\right)^2 J_1^2(\lambda_1 r)\right\} \\ & + \lambda_1 r\left(z+u_h\right)J_0(\lambda_1 r)J_1(\lambda_1 r)\left[1+\left(z+u_h\right)^2\right] \end{aligned} \tag{3.30}$$

Instead of attempting a second separable solution, we make use of an ansatz based on the non-homogeneous terms. Noting that all non-homogeneous terms can be seperated in orders of z, we hypothesize that ψ_1 may be written as

$$\psi_1 = R_a + zR_b + z^2 R_c + z^3 R_d \tag{3.31}$$

where R_a - R_d are functions of r alone. Substituting Eq. (3.31) into the left hand side of Eq. (3.30) and equating like powers of z we arrive at the following expressions

$$\begin{aligned} z^0\colon \quad & R_a''(r) - \frac{1}{r}R_a'(r) + \lambda_1^2 R_a(r) + 2R_c(r) = \frac{u_h J_1(\lambda_1 r)}{J_1^3(\lambda_1 r)} \left\{ -c_2^2 J_1^2(\lambda_1) r \right. \\ & -\lambda_1^2 r J_1^2(\lambda_1 r) \left[2 - u_h^2 \lambda_1^2 \right] + \lambda_1 J_0(\lambda_1 r) J_1(\lambda_1 r) \left[1 + u_h^2 \lambda_1^2 \right] \\ & \left. -u_h^2 r J_1^2(\lambda_1 r) \left[c_3^2 r^2 - \lambda_1^4 \right] \right\} \end{aligned} \tag{3.32}$$

$$\begin{aligned} z^1\colon \quad & R_b''(r) - \frac{1}{r}R_b'(r) + \lambda_1^2 R_b(r) + 6R_d(r) = -\frac{J_1(\lambda_1 r)}{J_1^3(\lambda_1)} \left\{ c_2^2 r \right. \\ & +\lambda_1^2 r J_0^2(\lambda_1 r) \left[2 - 3u_h^2 \lambda_1^2 \right] - J_0(\lambda_1 r) J_1(\lambda_1 r) \left[\lambda_1 + 3u_h^2 \lambda_1^3 \right] \\ & \left. +3u_h^2 r J_1^2(\lambda_1 r) \left[c_3^2 r^2 - \lambda_1^4 \right] \right\} \end{aligned} \tag{3.33}$$

$$\begin{aligned} z^2\colon \quad & R_c''(r) - \frac{1}{r}R_c'(r) + \lambda_1^2 R_c(r) = -\frac{3u_h J_1(\lambda_1 r)}{J_1^3(\lambda_1)} \left\{ c_3^2 r^3 J_1^2(\lambda_1 r) \right. \\ & \left. -\lambda_1^3 J_0(\lambda_1 r) J_1(\lambda_1 r) - \lambda_1^4 r \left[J_0^2(\lambda_1 r) + J_1^2(\lambda_1 r) \right] \right\} \end{aligned} \tag{3.34}$$

$$z^3\colon \quad R_d''(r) - \frac{1}{r}R_d'(r) + \lambda_1^2 R_d(r) = -\frac{J_1(\lambda_1 r)}{J_1^3(\lambda_1)}\left\{c_3^2 r^3 J_1^2(\lambda_1 r) \right.$$
$$\left. -\lambda_1^3 J_0(\lambda_1 r)J_1(\lambda_1 r) - \lambda_0^4 r\left[J_0^2(\lambda_1 r) + J_1^2(\lambda_1 r)\right]\right\} \quad (3.35)$$

Equations (3.32–3.35) represent two sets of one way coupled ordinary differential equations. As such, Eq. (3.34) and Eq. (3.35) can be solved for R_c and R_d whose solutions are then used in Eq. (3.32) and Eq. (3.33) to solve for R_a and R_b. Doing so yields

$$R_a(r) = rJ_1(\lambda_1 r)\left\{k_9 + \frac{\pi u_h}{2J_1^3(\lambda_1)}\left[\lambda_1 \mathcal{I}_5(r) + c_2^2 J_1^2(\lambda_1)\mathcal{I}_6(r) \right.\right.$$
$$\left.\left. -u_h^2\left\{\lambda_1^3 \mathcal{I}_1(r) - c_3^2 \mathcal{I}_2(r)\right\}\right] + \pi \mathcal{I}_7(r)\right\} + rY_1(\lambda_1 r)\left\{k_{10} + \frac{\pi u_h}{2J_1^3(\lambda_1)}\right.$$
$$\left. \times\left[\lambda_1 \mathcal{I}_8(r) - c_2^2 J_1^2(\lambda_1)\mathcal{I}_9(r) + u_h^2\left\{\lambda_1^3 \mathcal{I}_3(r) - c_3^2 \mathcal{I}_4(r)\right\}\right] - \pi \mathcal{I}_{10}(r)\right\} \quad (3.36)$$

$$R_b(r) = rJ_1(\lambda_1 r)\left\{k_{11} + \frac{\pi}{2J_1^3(\lambda_1)}\left[\lambda_1 \mathcal{I}_5(r) + c_2^2 J_1^2(\lambda_1)\mathcal{I}_6(r) \right.\right.$$
$$\left.\left. -3u_h^2\left\{\lambda_1^3 \mathcal{I}_1(r) - c_3^2 \mathcal{I}_2(r)\right\}\right] + 3\pi \mathcal{I}_{11}(r)\right\} + rY_1(\lambda_1 r)\left\{k_{12} + \frac{\pi}{2J_1^3(\lambda_1)}\right.$$
$$\left. \times\left[\lambda_1 \mathcal{I}_8(r) - c_2^2 J_1^2(\lambda_1)\mathcal{I}_9(r) + 3u_h^2\left\{\lambda_1^3 \mathcal{I}_3(r) - c_3^2 \mathcal{I}_4(r)\right\}\right] - 3\pi \mathcal{I}_{12}(r)\right\} \quad (3.37)$$

$$R_c(r) = rJ_1(\lambda_1 r)\left\{k_5 + \frac{3\pi u_h}{2J_1^3(\lambda_1)}\left[-\lambda_1^3 \mathcal{I}_1(r) + c_3^2 \mathcal{I}_2(r)\right]\right\}$$
$$+ rY_1(\lambda_1 r)\left\{k_6 + \frac{3\pi u_h}{2J_1^3(\lambda_1)}\left[\lambda_1^3 \mathcal{I}_3(r) - c_3^2 \mathcal{I}_4(r)\right]\right\} \quad (3.38)$$

$$\begin{aligned} R_d(r) = r J_1(\lambda_1 r) &\left\{ k_7 + \frac{\pi}{2 J_1^3(\lambda_1)} \left[-\lambda_1^3 \mathcal{I}_1(r) + c_3^2 \mathcal{I}_2(r) \right] \right\} \\ &+ r Y_1(\lambda_1 r) \left\{ k_8 + \frac{\pi}{2 J_1^3(\lambda_1)} \left[\lambda_1^3 \mathcal{I}_3(r) - c_3^2 \mathcal{I}_4(r) \right] \right\} \end{aligned} \tag{3.39}$$

where $\{\mathcal{I}_n(r); n = 1, 2, \ldots, 12\}$ represent straightforward integrals that cannot be expressed in closed form; defining them as special functions enables us to apply the first order boundary conditions analytically and then evaluate the special integrals numerically at the conclusion of the analysis. For the reader's convenience, our special integrals are specified in Appendix B. Finally, Eqs. (3.36–3.39) may be substituted back into Eq. (3.31) to obtain the first order stream function correction.

3.4.1 First Order Boundary Conditions

By examining condition (a) and then applying the second member of Eq. (3.21), we arrive at three equations that must hold in order to satisfy a vanishing radial velocity at the centerline $\forall z$. We therefore recover

$$\begin{aligned} -2k_{12} + 3\pi \Bigg\{ & 2k_7 \mathcal{I}_{10a}(0) + 2k_8 \mathcal{I}_{10d}(0) - \frac{1}{J_1^3(\lambda_1)} \left[\pi \lambda_1^3 \left(\mathcal{I}_{10b}(0) - \mathcal{I}_{10e}(0) \right) \right. \\ & \left. + c_3^2 \left(\pi \mathcal{I}_{10f}(0) - \pi \mathcal{I}_{10c}(0) - u_h^2 \mathcal{I}_4(0) \right) + u_h^2 \lambda_1^3 \mathcal{I}_3(0) + \tfrac{1}{3} \lambda_1 \mathcal{I}_8(0) \right] \Bigg\} \\ & + \frac{c_2^2 \pi \mathcal{I}_9(0)}{J_1(\lambda_1)} = 0 \end{aligned} \tag{3.40}$$

$$-2k_6 + \frac{3\pi u_h}{J_1^3(\lambda_1)} \left[-\lambda_1^3 \mathcal{I}_3(0) + c_3^2 \mathcal{I}_4(0) \right] = 0 \tag{3.41}$$

$$-3k_8 + \frac{3\pi}{2 J_1^3(\lambda_1)} \left[-\lambda_1^3 \mathcal{I}_3(0) + c_3^2 \mathcal{I}_4(0) \right] = 0 \tag{3.42}$$

Similarly, the radial velocity requirement at the sidewall Eq. (3.22) returns

$$-1 - 2k_{11}J_1(\lambda_1) - u_h^2\lambda_1^2 - 2k_{12}Y_1(\lambda_1) = 0 \tag{3.43}$$

$$-4k_5 J_1(\lambda_1) - 2u_h\lambda_1^2 - 4k_6 Y_1(\lambda_1) = 0 \tag{3.44}$$

$$-6k_7 J_1(\lambda_1) - \lambda_1^2 - 6k_8 Y_1(\lambda_1) = 0 \tag{3.45}$$

Lastly, the axial no-slip requirement in Eq. (3.23) leads to four equations that must be secured $\forall z$, specifically,

$$\begin{aligned}
&\tfrac{1}{2}\bigl\{2k_{10}\lambda_1 Y_0(\lambda_1) + c_2^2\pi u_h\mathcal{I}_6'(1) + 2\pi J_1(\lambda_1)\left[k_5 I_{7a}'(1) + k_6 I_{7d}'(1)\right] \\
&\quad + \frac{\pi u_h}{J_1^2(\lambda_1)}\bigl[u_h^2\bigl\{-\lambda_1^3\mathcal{I}_1'(1) + c_3^2\mathcal{I}_2'(1)\bigr\} + \lambda_1\mathcal{I}_5'(1) + 3\pi\bigl\{\lambda_1^3\left[I_{7e}'(1) - I_{7b}'(1)\right] \\
&\quad\quad + c_3^2\bigl[I_{7c}'(1) - I_{7f}'(1)\bigr]\bigr\}\bigr] + \frac{\pi Y_1(\lambda_1)}{J_1^3(\lambda_1)}\bigl[-2J_1^3(\lambda_1)\left\{k_5\mathcal{I}_{10a}'(1) + k_6\mathcal{I}_{10d}'(1)\right\} \\
&\quad\quad\quad + 3\pi\bigl\{\lambda_1^3\left[\mathcal{I}_{10b}'(1) - \mathcal{I}_{10e}'(1)\right] + c_3^2\bigl[\mathcal{I}_{10f}'(1) - \mathcal{I}_{10c}'(1)\bigr]\bigr\} \\
&\quad\quad\quad + u_h^3\bigl\{\lambda_1^3\mathcal{I}_3'(1) - c_3^2\mathcal{I}_4'(1)\bigr\} + u_h\lambda_1\mathcal{I}_8'(1) - c_2^2 u_h J_1^2(\lambda_1)\mathcal{I}_9'(1)\bigr]\bigr\} = 0
\end{aligned} \tag{3.46}$$

$$\begin{aligned}
&\tfrac{1}{2}\bigl\{2k_{12}\lambda_1 Y_0(\lambda_1) + c_2^2\pi\mathcal{I}_6'(1) + 6\pi J_1(\lambda_1)\left[k_7 I_{7a}'(1) + k_8 I_{7d}'(1)\right] \\
&\quad + \frac{\pi}{J_1^2(\lambda_1)}\bigl[u_h^2\bigl\{-3\lambda_1^3\mathcal{I}_1'(1) + 3c_3^2\mathcal{I}_2'(1)\bigr\} + \lambda_1\mathcal{I}_5'(1) + 3\pi\bigl\{\lambda_1^3\left[I_{7e}'(1) - I_{7b}'(1)\right] \\
&\quad\quad + c_3^2\bigl[I_{7c}'(1) - I_{7f}'(1)\bigr]\bigr\}\bigr] + \frac{\pi Y_1(\lambda_1)}{J_1^3(\lambda_1)}\bigl[-6J_1^3(\lambda_1)\left\{k_7\mathcal{I}_{10a}'(1) + k_8\mathcal{I}_{10d}'(1)\right\} \\
&\quad\quad\quad + 3\pi\bigl\{\lambda_1^3\left[\mathcal{I}_{10b}'(1) - \mathcal{I}_{10e}'(1)\right] + c_3^2\bigl[\mathcal{I}_{10f}'(1) - \mathcal{I}_{10c}'(1)\bigr]\bigr\} \\
&\quad\quad\quad + 3u_h^2\bigl\{\lambda_1^3\mathcal{I}_3'(1) - c_3^2\mathcal{I}_4'(1)\bigr\} + \lambda_1\mathcal{I}_8'(1) - c_2^2 J_1^2(\lambda_1)\mathcal{I}_9'(1)\bigr]\bigr\} = 0
\end{aligned} \tag{3.47}$$

$$k_6\lambda_1 Y_0(\lambda_1) + \frac{3\pi u_h}{2J_1^3(\lambda_1)} \left\{ J_1(\lambda_1) \left[-\lambda_1^3 \mathcal{I}_1'(1) + c_3^2 \mathcal{I}_2'(1) \right] \right.$$
$$\left. + Y_1(\lambda_1) \left[\lambda_1^3 \mathcal{I}_3'(1) - c_3^2 \mathcal{I}_4'(1) \right] \right\} = 0 \quad (3.48)$$

$$k_8\lambda_1 Y_0(\lambda_1) + \frac{\pi}{2J_1^3(\lambda_1)} \left\{ J_1(\lambda_1) \left[-\lambda_1^3 \mathcal{I}_1'(1) + c_3^2 \mathcal{I}_2'(1) \right] \right.$$
$$\left. + Y_1(\lambda_1) \left[\lambda_1^3 \mathcal{I}_3'(1) - c_3^2 \mathcal{I}_4'(1) \right] \right\} = 0 \quad (3.49)$$

Equations (3.40–3.49) represent a system of 10 equations. However, c_3^2 is doubly constrained and k_9 is not present in the system. As such, Eq. (3.41) and Eq. (3.48) may be solved for k_6 and c_3^2, the results of which can then be inserted into Eq. (3.44) to retrieve k_5. In like manner, Eq. (3.42), Eq. (3.49), and Eq. (3.45) can be solved for k_7 and k_8 with an identical result for c_3^2. Subsequently, Eq. (3.40), Eq. (3.46), and Eq. (3.47) may be resolved to obtain k_{10}, k_{12}, and c_2^2, at which point Eq. (3.43) will yield k_{11}. Finally, the condition at the headwall Eq. (3.24) can be applied to obtain k_9. These steps complete the determination of the first order streamfunction correction ψ_1. In what follows, a comparison to the compressible, non-swirling, Taylor-Culick flow analog [21] will be performed while examining the dilatational effects induced by the compressible correction.

3.5 Results and Discussion

3.5.1 Velocity Profile Comparison

With the stream function and density in hand, all remaining flow attributes may be readily determined. We focus on a specific heat ratio of $\gamma = 1.4$ and an injection Mach number of $M_w = 0.01$. The spatial evolution of the axial and radial velocity components corresponding to $u_h = 0$ for the compressible Trkalian model as well as the compressible Taylor-Culick solution [21] are illustrated side-by-side in Fig. 3.1. In both models, the axial velocities exhibit gradual steepening near the wall in agreement with previous studies (Figs. 3.1a–3.1b). In contrast to the Taylor-Culick profile, the Trkalian motion exhibits a decrease in centerline speed relative to its incompressible counterpart; we find that the profile thickens considerably as the locus of the maximum axial velocity pushes outwardly toward the sidewall. It thus mimics the behavior of the compressible bidirectional vortex in its core region [31]. Nonetheless, the Trkalian axial velocity remains ahead of its Taylor-Culick counterpart at all axial stations examined. This can be attributed to the increased kinetic energy that accompanies the Trkalian motion [29]. Interestingly, noticeable dilatational effects are not seen in either model until a chamber length of $z = 15$.

The radial components of velocity for both models are illustrated in Figs. 3.1c–3.1d. Here, we see a favorable agreement between both Trkalian and complex lamellar models, as their radial profiles flatten with increasing distance from the headwall. Appreciable effects can be seen much closer to the headwall than in the case of the axial profile, and can be partially attributed to the incompressible radial speed

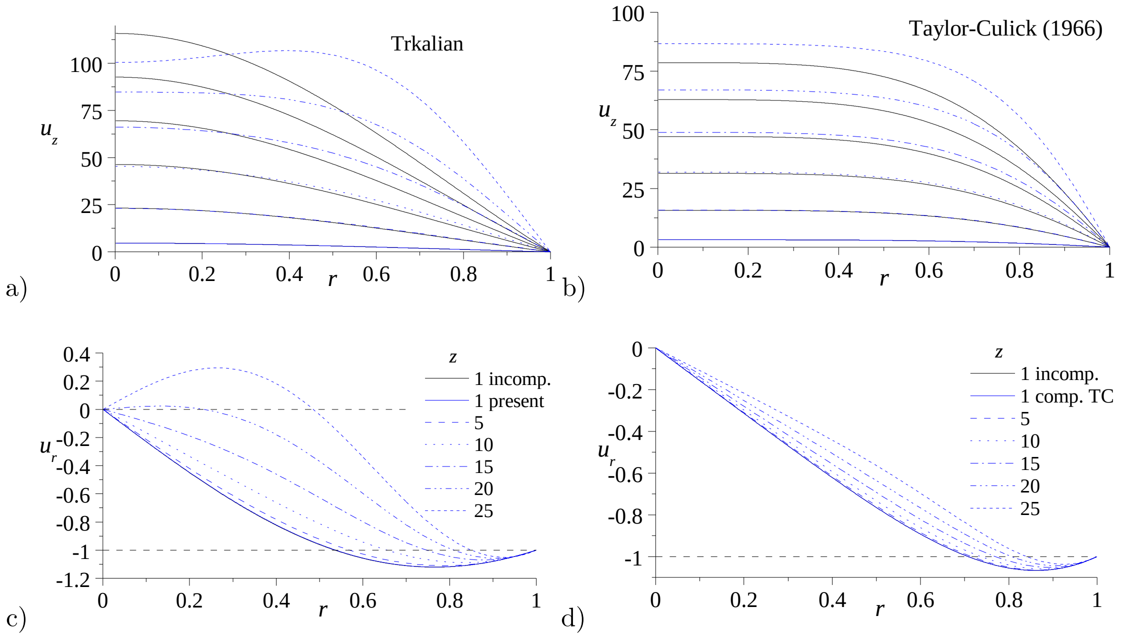

Figure 3.1. Spatial evolution of (a-b) axial and (c-d) radial velocity components with $M_w = 0.01$, $\gamma = 1.4$, and $u_h = 0$ using either Trkalian (left) or Taylor-Culick profiles (right).

remaining axially invariant in both models. In the case of the Trkalian model the radial component acquires a positive or outward velocity as $r \to 0$ at the finite actual stations of $z = 20$ and 25 depitcted in Fig. 3.1c. This reversal in polarity corresponds to the dip in u_z near the core for the same axial stations. Overall, the effects on the radial profile are much more pronounced than what is seen in the Taylor-Culick model. In fact, it can be shown that the compressible Taylor-Culick profile will exhibit similar behavior at a farther distance. Owing to the higher kinetic energy that accompanies the Trkalian flowfield, it is understandable that its dilatational effects play a larger role much sooner in the chamber.

The swirl component of velocity, which is unique to this rocket flow configuration, is illustrated in Fig. 3.2 for $M_w = 0.005$ and $M_w = 0.01$, where the effect of wall injection is examined. Here too, it may be instructive to note that the tangential velocity component does not vanish at the sidewall. The tangential slip in $u_\theta(1, z)$ may be attributed to the inviscid nature of the problem. In reality, the profile will dip sharply at the sidewall to a value of zero due to the incompressible, viscous boundary layer, whose analysis will be presented in future work. However, owing to the judicious assortment of boundary conditions placed on the axial and radial speeds, both components prove to satisfy the velocity-adherence requirement to the extent of appearing quasi-viscous in their spatial distributions. Furthermore, the curvatures of the compressible u_θ profiles seem to gradually flatten near the core region as the flow progresses downstream before crossing over its incompressible counterpart as $r \to 1$. This behavior is clearly depicted in Fig. 3.2b where the profile at $z = 25$ undergoes a slight depression in the core before recovering steeply to a value exceeding its incompressible counterpart near the wall. It should also be noted that the slow growth of u_θ near $r = 0$ mirrors the magnitude reduction that we saw earlier in u_z within the core region (Fig. 3.1a). The near wall overshoot of the compressible solution at higher Mach numbers seems to be a salient feature of both u_θ and u_z. As in the case of the axial motion, appreciable dilatational effects are not observed until an axial location of $z = 15$ or 10 for $M_w = 0.005$ and 0.01, respectively. Clearly, a larger wall Mach number precipitates compressibility-based deviations at an earlier location. Due to the use of M_w as the perturbation parameter, it may be ascertained that an increase in the wall injection Mach number promotes wider deviations between the compressible and incompressible models, thus confirming that the compressible

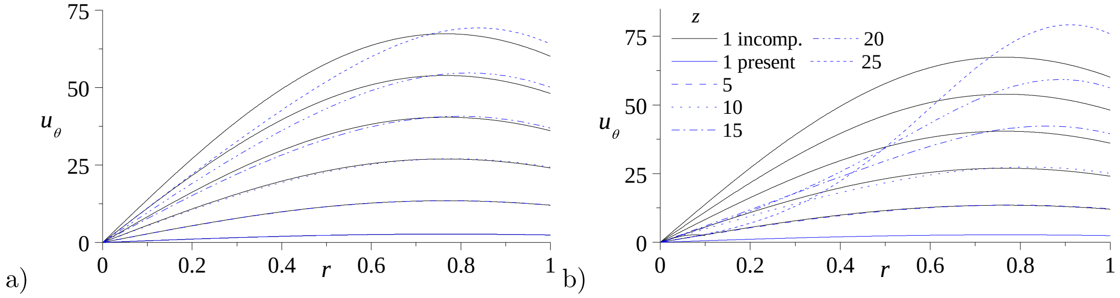

Figure 3.2. Radial distribution of the compressible swirl velocity, u_θ, at several axial stations using $u_h = 0$ and a wall injection Mach number M_w of either a) 0.005 or b) 0.01.

correction will play a larger role in the overall flow description as the wall injection Mach number is increased.

3.5.2 Thermodynamic Variables

While the pressure and temperature corrections may be retrieved rather straightforwardly from the isentropic relations, i.e.

$$p_1 = \gamma \rho_1 \qquad \text{and} \qquad T_1 = (\gamma - 1)\, \rho_1 \tag{3.50}$$

the first order density may be readily evaluated from Eq. (3.29). To study their behavior, the density and temperature profiles are illustrated in Fig. 3.3 for $u_h = 0$ and several axial stations. The graphical parallelism that emerges in the ensuing distributions may be attributed to the mathematical expressions for the temperature and pressure corrections as they differ from the density by only a constant. Because $\gamma \in [1.1, 1.67]$ always exceeds unity, its presence in Eq. (3.50) leads to a modest amplification in the pressure correction and a conjugate reduction in the first order temperature relative to ρ_1. These proportions may be visually inferred when comparing the density in Fig. 3.3a to the temperature in Fig. 3.3b, and then the pressure in Fig. 3.4a.

In Fig. 3.4b, the evolution of the centerline pressure is also compared to several mathematical models found in the literature in addition to two previously reported CFD simulations [21]. While good agreement is observed near the headwall, the compressible Trkalian model seems to diminish at a faster rate than the other featured solutions to the extent of overshooting the turbulent models by approximately 10%; conversely, one may realize that the compressible Taylor-Culick profile by Majdalani [21] undershoots the CFD simulations by a comparable amount of nearly 10%. The overshooting of the Trkalian pressure relative to the CFD simulations can be attributed to, on the one hand, its higher centerline velocity and, on the other hand, swirl being suppressed in the simulations referenced here. Evidently, the theoretical pressure associated with the higher kinetic energy Trkalian flowfield will be lower than its Taylor-Culick counterpart at a given axial station. The larger drop in pressure is also consistent with the leading-order behavior dictated by the incompressible Trkalian profile [29]. Finally, a numerical simulation that does not prevent swirl from developing may be more appropriate to use as a benchmark in future analysis.

3.5.3 Critical Distance or Sonic Length

With the temperature in hand, the speed of sound may be readily calculated, and this enables us to specify the sonic distance as the range from the headwall to the point where the maximum axial speed first crosses the speed of sound barrier.

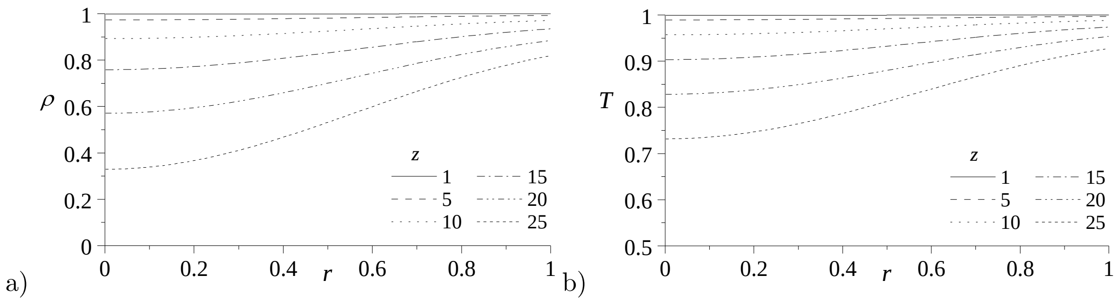

Figure 3.3. Radial distribution of compressible a) density, ρ, and b) temperature, T, at several axial stations using $u_h = 0$ and $\gamma = 1.4$.

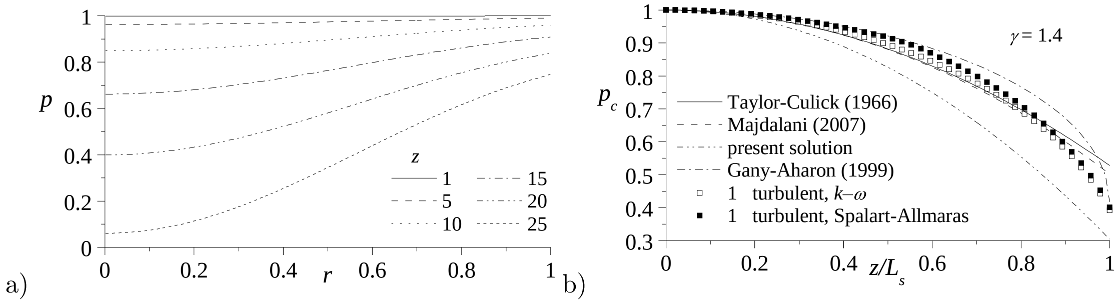

Figure 3.4. Spatial variation of the pressure at a) several axial stations as function of r and b) the chamber centerline pressure as function of the axial distance z (normalized by the sonic length) using several compressible models and two turbulent flow simulations.

The corresponding sonic length may be determined by letting

$$\bar{u}_z(\bar{r}_{\max}, \bar{L}_s) = \sqrt{\gamma R \bar{T}} \qquad \text{or} \qquad M_w u_z(\bar{r}_{\max}, \bar{L}_s) = \sqrt{T} \tag{3.51}$$

where $\bar{r}_{\max}$ denotes the radial location of the maximum axial velocity and where T must be evaluated as well to ensure that the evolving local speed of sound is being used as a reference. Due to the inherent complexity of the ensuing expression, the search for the proper root is handled numerically. At the outset, tabulated values of the dimensionless sonic length, $L_s = \bar{L}_s/a$, are posted in Table 3.1 for a range of wall injection Mach numbers of $(0.005, 0.006, 0.007, 0.008, 0.009, 0.01)$, three headwall injection coefficients of $u_h = (0, 0.5, 10)$, and three specific heat ratios of $\gamma = (1.2, 1.4, 1.6)$. As one expects, the sonic length decreases for increasing M_w, u_h, and γ. While the first two parameters cause the flow to accelerate, a larger ratio of specific heats leads to a larger temperature drop and, consequently, a smaller speed of sound. One case of interest corresponds to $M_w = 0.01$, $\gamma = 1.4$, and $u_h = 0$, where L_s is calculated to be 21.532. This computed value falls below the corresponding sonic length for the compressible Taylor-Culick model by 21%, since in the latter case $L_s = 26.145$ according to Majdalani [21]. A lower value for the sonic length may be anticipated considering that the maximum axial velocity of the compressible Trkalian model always leads in the streamwise direction its Taylor-Culick flow analog. For this reason, the Trkalian axial velocity reaches sonic conditions sooner than its Taylor-Culick counterpart. Beyond the sonic point, it may be argued that the main assumptions that stand behind the present framework may begin to deteriorate because of the inevitable onset of shocks and irreversible losses. In practice though, both Kaplan [37] and Tollmien [38] report excellent agreement with numerical simulations downstream of the choking plane when a rigorous Rayleigh-Janzen expansion is employed. In fact, both Majdalani [21] and Maicke and Majdalani [22] arrive at similar conclusions in their investigations of the compressible, non-swirling Taylor-Culick family of problems. Therein, the use of L_s as a normalizing length is shown to produce an invaluable, quasi-frozen, universal representation of the stream function and its derivatives. Here too, we find that a suitably normalized axial coordinate gives rise to an essentially Mach number independent similarity solution. To

Table 3.1. Sonic length, L_s, over a range of Mach numbers and three values of γ and u_h

γ	$M_w =$	0.005	0.006	0.007	0.008	0.009	0.01
	$u_h = 0$						
1.2		45.330	37.779	32.387	28.343	25.198	22.684
1.4		43.048	35.878	30.756	26.912	23.915	21.532
1.6		41.630	34.298	29.117	25.360	23.003	20.297
	$u_h = 0.5$						
1.2		44.836	37.287	31.859	27.852	24.706	22.195
1.4		42.551	35.384	30.269	26.421	23.430	21.045
1.6		41.082	33.300	28.474	24.855	22.041	19.789
	$u_h = 10$						
1.2		35.284	27.713	22.296	18.224	15.047	12.497
1.4		32.991	25.795	20.640	16.747	13.698	11.285
1.6		30.507	24.217	19.015	15.231	11.710	10.096

illustrate this behavior, the self-similarity in question is showcased in the port plots of Fig. 3.5, where the downstream evolutions of all three components of the velocity are featured for $0.001 \leq M_w \leq 0.01$. Despite the use of different wall injection Mach numbers, the normalized solutions prove to be visually indiscernible. For example, although Fig. 3.5 is produced at $M_w = 0.01$, it is equally representative of the velocities computed at an order of magnitude smaller injection Mach number. Given that the three developing components of velocity are shown in close proximity, it is evident that dilatational effects have the most visible impact on the radial velocity profiles. Moreover, we find that the flattening of the axial velocity, which is originally prescribed by a Bessel function, brings the solution closer to both CFD and laboratory measurements reported by various numerical analysts and experimentalists [39, 40, 12, 41, 14, 13, 42, 43, 44].

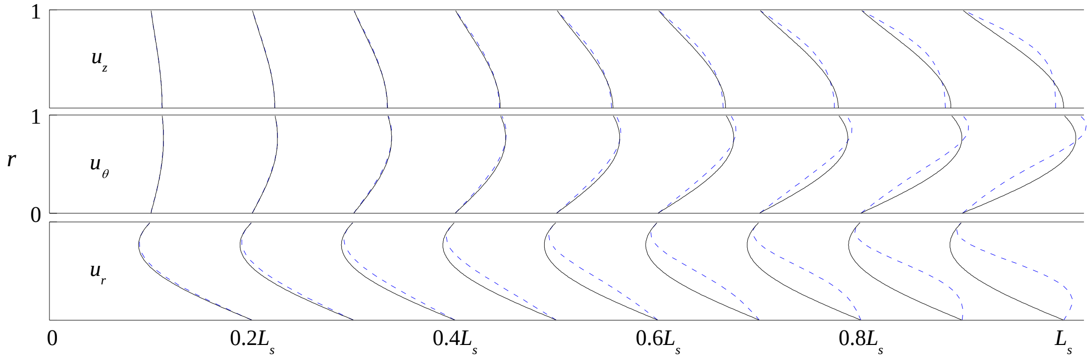

Figure 3.5. Spatial evolution of axial, tangential, and radial velocity components up to the sonic length L_s. Because of the self-similarity with respect to L_s, the velocity distributions remain indiscernible over a wide range of wall Mach numbers ($0.001 \leq M_w \leq 0.01$).

3.5.4 Velocity Ratios

In an effort to further characterize the role of compressibility on the flowfield, several velocity ratios are examined for $0 \leq r \leq 1$. In delving deeper into the effects of density variations and their spatial influence on the motion, we use Fig. 3.6 to quantify the ratio of compressible-to-incompressible magnitudes for the axial and tangential velocities at five equidistant axial stations extending from the headwall to the sonic length. This comparison is drawn at two values of u_h that are representative of either a solid rocket motor with no headwall injection, or a hybrid chamber with an equivalent $u_h = 10$. For the axial speed ratio in Fig. 3.6a, it is easy to spot the inner zone ranging over $0 \leq r \leq 0.26$ for $u_h = 0$, where the compressible velocity drops below its incompressible counterpart. More noticeably perhaps is the amplification of this ratio in the outer zone, i.e., $0.26 \leq r \leq 1$ for $u_h = 0$, where dilatational effects lead to a substantial increase in axial speed. Interestingly, at the centerline of the downstream section of our domain, where $r = 0$ and $z = L_s$, a flattening of the

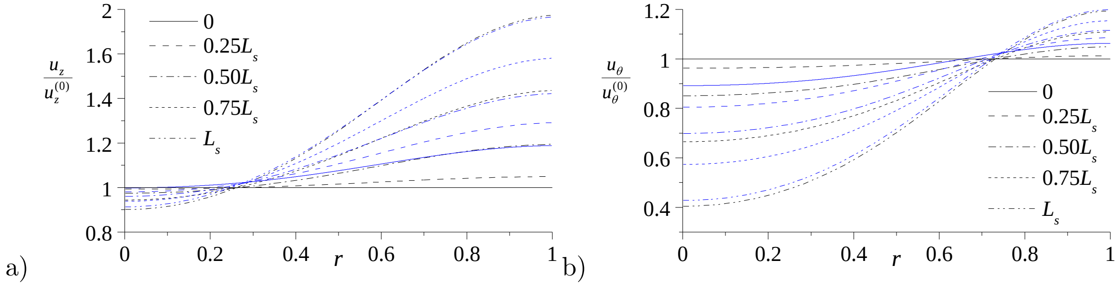

Figure 3.6. Effects of compressibility on the flowfield variables as captured by the compressible-to-incompressible velocity ratios for a) u_z and b) u_θ. In the above, black and blue lines correspond to either $u_h = 0$ (SRM) or $u_h = 10$ (HRE).

compressible velocity may be detected in both cases of u_h, as u_z dips to approximately 90% of its incompressible counterpart. Conversely, we find that u_z reaches nearly 178% of the incompressible velocity as $r \to 1$. For both the axial and tangential profiles, the effect of headwall injection becomes inconsequential as the distance from the headwall is continually increased. The largest difference occurs at the headwall where the axial velocity vanishes for the case of $u_h = 0$ but remains finite for $u_h = 10$. After the initial jump for the case of $u_h = 10$, the spatial evolution over subsequent axial stations leads to a gradual reduction in the deviations between the two cases, thus allowing the velocity ratio with no headwall injection to eventually match that for $u_h = 10$ at $z = L_s$. As for the tangential velocity ratio, the compressible u_θ is reduced to approximately 40% of its incompressible value at the centerline and is seen to reach only 119% of its incompressible expression as $r \to 1$. The magnification of u_θ is similarly captured in the outer annular zone extending over the range $0.73 \leq r \leq 1$ for $u_h = 0$. Inside this circle, the effects of fluid compression lead to a decrease in u_θ.

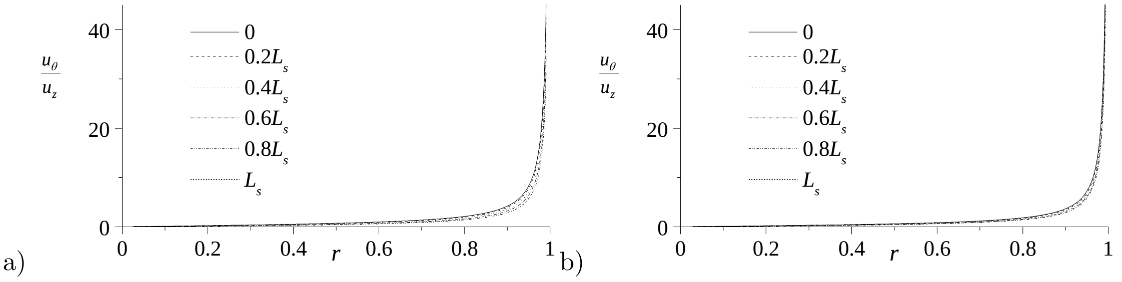

Figure 3.7. Axial development of the tangential-to-axial velocity ratio for a) $u_h = 0$ and b) $u_h = 10$.

Before leaving this section, and to better understand the order of the swirl velocity relative to the main axial motion, we find it useful to quantify the tangential-to-axial velocity ratio under high speed conditions. This ratio is depicted in Fig. 3.7 for several axial stations and values of u_h. At the centerline, the ratio begins at zero because of the vanishing of u_θ, and then increases rapidly as r approaches the sidewall, thus indicating a role reversal in u_z, which under-performs u_θ in the vicinity of the sidewall. The steep behavior that we observe as $r \to 1$ in Fig. 3.7 is somewhat misleading, as it may be attributed to the vanishing of u_z at the sidewall despite the presence of a finite u_θ. We recall that by virtue of the underlying inviscid assumption used throughout this study, the no-slip condition at the sidewall is still fulfilled in the axial direction as $u_z \to 0$ at $r \to 1$; in contrast, u_θ does not (yet) satisfy the velocity-adherence requirement at the sidewall. In reality, one must also ensure that $u_\theta \to 0$ as $r \to 1$, in view of the viscous boundary layer that inevitably forms at the sidewall. The steep behavior in Fig. 3.7 is therefore artificial, and would not have materialized had the tangential velocity been treated asymptotically and compelled to secure the no-slip condition at the wall. Yet irrespective of the models used, we find very small deviations in this ratio at successive axial stations. The weak spatial sensitivity of

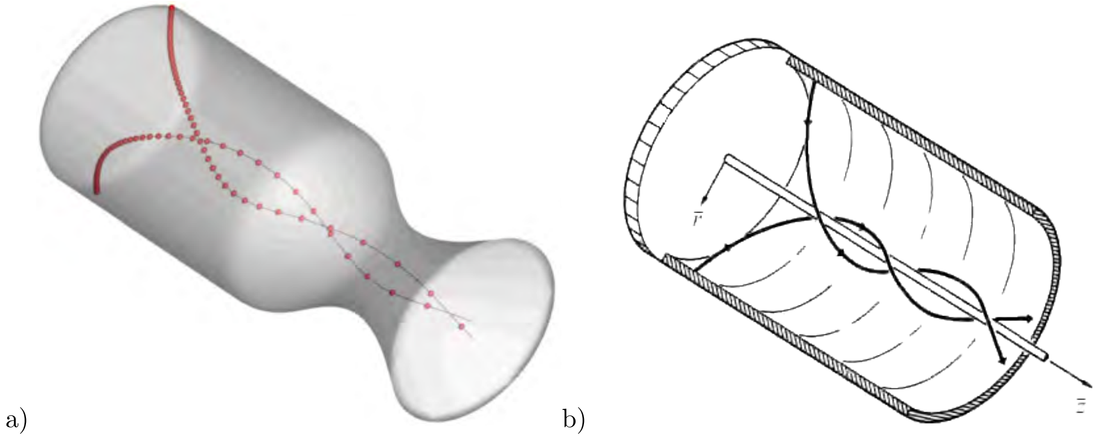

Figure 3.8. Schematic renderings of a) the compressible Trkalian streaklines and b) those observed by Dunlap et al. [13]

u_θ/u_z may be attributed to the self-cancelling spatial linearity of the leading order axial and tangential velocities with respect to z, unlike the first order corrections, which exhibit a weaker cubic dependence. Finally, we find minor deviations in our profiles as u_h is increased, apart from a modest bulging of the solution outwardly due to the thickening of the axial profile as a larger mass flux is introduced at the headwall.

3.6 Conclusions

In this study, the compressible form of the helical Trkalian model is derived in a semi-analytical form. Other compressible flow investigations, such as the compressible Taylor-Culick profile [21], do not support the evolution of a tangential component of velocity. However, experimental studies by Dunlap et al. [13, 14] along with theoretical analyses by Balachandar et al. [15] suggest that in some smooth cylindrically-shaped rocket chambers, a swirling motion evolves naturally. In this chapter, the efforts of Majdalani and Fist [29] at specifying this swirling motion are systematically extended to capture the dilatational effects on the Trkalian motion. Our model appears to be quite realistic when qualitatively compared to the results of Dunlap et al. [13] as shown side-by-side in Fig. 3.8.

By comparing our new findings to available models, the effects of compressibility are quantified in the presence of a high kinetic energy Trkalian flowfield. In this vein, the steepening of our axial profile near the sidewall appears to be in agreement with former studies, especially that the dilatational effects on the radial velocity resemble those of the compressible Taylor-Culick model, with the notable difference of becoming more appreciable as the distance from the headwall is increased. Given the higher kinetic energy content of this new helical solution, disparities from the complex-lamellar flow analog are realized, and these include a more pronounced flattening of the core axial velocity, and a slight overshoot in all three components of the velocity field as the sidewall is approached. At the outset, steeper wall gradients are produced, as one fully expects. Interestingly, this flow distortion is accompanied by a reversal in the radial flow velocity as the sonic length is approached. A similar reversal is undertaken at a later distance by the slower, compressible Taylor-Culick profile downstream of the sonic point.

In addition to the dilatational effects on the axial, radial, and tangential velocities, we quantify in this study the spatial evolution of the pressure, density, and temperature distributions. Along similar lines, we numerically evaluate the sonic length, an important scaling parameter over which our solution remains valid, and show that it exhibits the correct behavior when compared to other, less energetic mean flow approximations. Furthermore, as the Trkalian centerline pressure is compared to several existing solutions, it is seen to overshoot two computational predictions at the chamber exit, unlike the compressible Taylor-Culick counterpart, which underpredicts simulation results by an equal amount (10% approximately). Our findings also indicate that the distance from the headwall to the sonic point can serve as a valuable reference lengthscale to normalize the axial coordinate: the renormalized solution becomes quasi-frozen and fundamentally Mach number independent. Finally, in seeking to determine the net flow magnification or compression caused by high speed motion, the compressible-to-incompressible velocity ratios are characterized over the entire domain of interest for both the axial and tangential velocities, thus showing significant distortions, especially in the axial velocity, for sufficiently long chambers or high injection speeds.

While the present model captures many useful aspects of swirling SRM and HRE flowfields, a viscous correction at the sidewall remains essential to properly resolve the tangential velocity as $r \to 1$. In fact, an asymptotic treatment of the three-dimensional wall boundary layers will be imperative to ensure that the no-slip requirement is met at the sidewall in all three spatial directions. Once the boundary layers are accounted for, it becomes possible to not only evaluate the shear stresses, the skin friction coefficient, and the torques applied to the motor casing, but also to use the Reynolds transport analogy to estimate the heat transfer properties of the swirling fluid. Additional variations that we plan on pursuing in future work include replacing the uniform radial injection speed at the sidewall with a uniform mass flux, and substituting the isentropic state relations with the energy equation. Moreover, the advent of a compressible, swirl-capable, bulk gaseous motion for solid and hybrid rockets may be viewed as critically important because not only does it increase our repertoire of engineering approximations for rocket chambers and porous tubes, but it will also enable us to investigate the hydrodynamic instability of the mean flowfield using a consistently compressible solution, reformulate our description of the vortico-acoustic wave problem in the presence of swirl, and recast the framework that was formerly used to capture particle-mean flow interactions. It is clear that the present analysis opens up several well-defined and closely intertwined lines of research inquiry.

Bibliography

[1] Culick, F. E. C., "Rotational Axisymmetric Mean Flow and Damping of Acoustic Waves in a Solid Propellant Rocket," *AIAA Journal*, Vol. 4, No. 8, 1966, pp. 1462–1464. doi:10.2514/3.3709.

[2] Flandro, G. A., Fischbach, S. R., and Majdalani, J., "Nonlinear Rocket Motor Stability Prediction: Limit Amplitude, Triggering, and Mean Pressure Shift," *Physics of Fluids*, Vol. 19, No. 9, September 2007, pp. 094101–16. doi:10.1063/1.2746042.

[3] Fischbach, S. R., Majdalani, J., and Flandro, G. A., "Acoustic Instability of the Slab Rocket Motor," *Journal of Propulsion and Power*, Vol. 23, No. 1, January-February 2007, pp. 146–157. doi:10.2514/1.14794.

[4] Fischbach, S. R., Flandro, G. A., and Majdalani, J., "Acoustic Streaming in Simplified Liquid Rocket Engines with Transverse Mode Oscillations," *Physics of Fluids*, Vol. 22, No. 6, June 2010, pp. 063602–21. doi:10.1063/1.3407663.

[5] Féraille, T., and Casalis, G., "Channel Flow Induced by Wall Injection of Fluid and Particles," *Physics of Fluids*, Vol. 15, No. 2, February 2003, pp. 348–360. doi:10.1063/1.1530158.

[6] Bhatia, L., Abu-Irshaid, E. M., Majdalani, J., and Casalis, G., "Stability of the Taylor-Culick Profile with Headwall Injection and Particle Interactions," *42th AIAA/ASME/SAE/ASEE Joint Propulsion Conference and Exhibit*, AIAA Paper 2006-4429, Sacramento, CA, July 2006. doi:10.2514/6.2006-4429.

[7] Féraille, T., Casalis, G., and Dupays, J., "Particle Effects on Solid-Propellant Motors Flow Stability," *40th AIAA/ASME/SAE/ASEE Joint Propulsion Conference and Exhibit*, AIAA Paper 2002-3611, Fort Lauderdale, FL, July 2002. doi:10.2514/6.2002-3611.

[8] Ugurtas, B., Avalon, G., Lupoglazoff, N., Vuillot, F., and Casalis, G., *Stability and Acoustic Resonance of Internal Flows Generated by Side Injection*, Vol.

185, AIAA Progress in Astronautics and Aeronautics, Washington, DC, 2000, pp. 823–836.

[9] Fabignon, Y., Dupays, J., Avalon, G., Vuillot, F., Lupoglazoff, N., Casalis, G., and Prévost, M., "Instabilities and Pressure Oscillations in Solid Rocket Motors," *Journal of Aerospace Science and Technology*, Vol. 7, No. 3, April 2003, pp. 191–200. doi:10.1016/S1270-9638(02)01194-X.

[10] Boyer, G., Casalis, G., and Estivalèzes, J. L., "Stability and Sensitivity Analysis in a Simplified Solid Rocket Motor Flow," *Journal of Fluid Mechanics*, Vol. 722, 2013, pp. 618–644. doi:10.1017/jfm.2013.90.

[11] Boyer, G., Casalis, G., and Estivaèzes, J. L., "Stability Analysis and Numerical Simulation of Simplified Solid Rocket Motors," *Physics of Fluids*, Vol. 25, No. 8, 2013, pp. 084109–084109. doi:10.1063/1.4818552.

[12] Majdalani, J., "Helical Solutions of the Bidirectional Vortex in a Cylindrical Cyclone: Beltramian and Trkalian Motions," *Fluid Dynamics Research*, Vol. 44, No. 6, October 2012, pp. 065506–38. doi:10.1088/0169-5983/44/6/065506.

[13] Dunlap, R., Blackner, A. M., Waugh, R. C., Brown, R. S., and Willoughby, P. G., "Internal Flow Field Studies in a Simulated Cylindrical Port Rocket Chamber," *Journal of Propulsion and Power*, Vol. 6, No. 6, 1990, pp. 690–704. doi:10.2514/3.23274.

[14] Dunlap, R., Sabnis, J. S., Beddini, R. A., Flandro, G. A., Brown, R. S., Gibeling, H. J., Blackner, A. M., Waugh, R. C., and McDonald, H., "Internal Flow Field Investigation," Tech. Rep. TR-85-079, U. S. Air Force Rocket Propulsion Laboratory, August 1985.

[15] Balachandar, S., Buckmaster, J. D., and Short, M., "The Generation of Axial Vorticity in Solid-Propellant Rocket-Motor Flows," *Journal of Fluid Mechanics*, Vol. 429, No. 1, February 2001, pp. 283–305. doi:10.1017/S0022112000002688.

[16] Majdalani, J., and Akiki, M., "Rotational and Quasiviscous Cold Flow Models for Axisymmetric Hybrid Propellant Chambers," *Journal of Fluids Engineering*, Vol. 132, No. 10, 2010, pp. 101202–7. doi:10.1115/1.4002397.

[17] Xu, H., Lin, Z. L., Liao, S. J., Wu, J. Z., and Majdalani, J., "Homotopy Based Solutions of the Navier-Stokes Equations for a Porous Channel with Orthogonally Moving Walls," *Physics of Fluids*, Vol. 22, No. 5, May 2010, pp. 05360101–18. doi:10.1063/1.3392770.

[18] Majdalani, J., Vyas, A. B., and Flandro, G. A., "Higher Mean-Flow Approximation for a Solid Rocket Motor with Radially Regressing Walls," *AIAA Journal*, Vol. 40, No. 9, September 2002, pp. 1780–1788. doi:10.2514/2.1854.

[19] Majdalani, J., Vyas, A. B., and Flandro, G. A., "Erratum on Higher Mean-Flow Approximation for a Solid Rocket Motor with Radially Regressing Walls," *AIAA Journal*, Vol. 47, No. 1, September 2009, pp. 286–286. doi:10.2514/1.40061.

[20] Kurdyumov, V. N., "Steady Flows in the Slender, Noncircular, Combustion Chambers of Solid Propellants Rockets," *AIAA Journal*, Vol. 44, No. 12, December 2006, pp. 2979–2986. doi:10.2514/1.21125.

[21] Majdalani, J., "Analytical Models for Hybrid Rockets," *Fundamentals of Hybrid Rocket Combustion and Propulsion*, edited by K. Kuo and M. J. Chiaverini, Progress in Astronautics and Aeronautics, chap. Chap. 5, AIAA Progress in Astronautics and Aeronautics, Washington, DC, 2007, pp. 207–246.

[22] Maicke, B. A., and Majdalani, J., "On the Rotational Compressible Taylor Flow in Injection-Driven Porous Chambers," *Journal of Fluid Mechanics*, Vol. 603, No. 1, April 2008, pp. 391–411. doi:10.1017/S0022112008001122.

[23] Majdalani, J., and Saad, T., "The Taylor-Culick Profile with Arbitrary Headwall Injection," *Physics of Fluids*, Vol. 19, No. 9, September 2007, pp. 093601–10. doi:10.1063/1.2746003.

[24] Saad, T., and Majdalani, J., "Rotational Flowfields in Porous Channels with Arbitrary Headwall Injection," *Journal of Propulsion and Power*, Vol. 25, No. 4, July-August 2009. doi:10.2514/1.41926.

[25] Traineau, J. C., Hervat, P., and Kuentzmann, P., "Cold-Flow Simulation of a Two-Dimensional Nozzleless Solid-Rocket Motor," *22nd AIAA/ASME/SAE/ASEE Joint Propulsion Conference*, AIAA Paper 86-1447, Huntsville, AL, June 1986. doi:10.2514/6.1986-1447.

[26] Balakrishnan, G., Liñan, A., and Williams, F. A., "Rotational Inviscid Flow in Laterally Burning Solid Propellant Rocket Motors," *Journal of Propulsion and Power*, Vol. 8, No. 6, November-December 1992, pp. 1167–1176. doi:10.2514/3.11458.

[27] Akiki, M., and Majdalani, J., "Exact Solutions for the Integral Form of the Compressible Flowfield in a Porous Cylinder," *47th AIAA/ASME/SAE/ASEE*

Joint Propulsion Conference and Exhibit, AIAA Paper 2011-5953, San Diego, CA, July-August 2011. doi:10.2514/6.2011-5953.

[28] Akiki, M., and Majdalani, J., "Improved Integral Form of the Compressible Flowfield in Thin Channels with Injection," *AIAA Journal*, Vol. 50, No. 2, February 2012, pp. 485–493. doi:10.2514/1.J051282.

[29] Majdalani, J., and Fist, A., "Improved Mean Flow Solution for Solid Rocket Motors with a Naturally Developing Swirling Motion," *50th AIAA/ASME/SAE/ASEE Joint Propulsion Conference and Exhibit*, AIAA Paper 2014-4016, Cleveland, OH, July 2014. doi:10.2514/6.2014-4016.

[30] Maicke, B. A., and Majdalani, J., "On the Compressible Bidirectional Vortex. Part 1: A Bragg-Hawthorne Stream Function Formulation," *50th AIAA Aerospace Sciences Meeting including the New Horizons Forum and Aerospace Exposition*, AIAA Paper 2012-1103, Nashville, TN, January 2012. doi:10.2514/6.2012-1103.

[31] Maicke, B. A., and Majdalani, J., "On the Compressible Bidirectional Vortex. Part 2: A Beltramian Flowfield Approximation," *50th AIAA Aerospace Sciences Meeting including the New Horizons Forum and Aerospace Exposition*, AIAA Paper 2012-1104, Nashville, TN, January 2012. doi:10.2514/6.2012-1104.

[32] Bragg, S. L., and Hawthorne, W. R., "Some Exact Solutions of the Flow through Annular Cascade Actuator Disks," *Journal of the Aeronautical Sciences*, Vol. 17, No. 4, 1950, pp. 243–249.

[33] Cecil, O., and Majdalani, J., "On Steady Trkalian High Speed Flows: Swirling Compressible Motions in Rockets with Headwall Injection," *51st AIAA/ASME/SAE/ASEE Joint Propulsion Conference and Exhibit*, AIAA Paper 2015-3788, Orlando, FL, 2015. doi:10.2514/6.2015-3788.

[34] Abu-Irshaid, E. M., Majdalani, J., and Casalis, G., "Hydrodynamic Stability of Rockets with Headwall Injection," *Physics of Fluids*, Vol. 19, No. 2, February 2007, pp. 024101–11. doi:10.1063/1.2434797.

[35] Kurdyumov, V. N., "Viscous and Inviscid Flows Generated by Wall-Normal Injection into a Cylindrical Cavity with a Headwall," *Physics of Fluids*, Vol. 20, No. 12, December 2008, pp. 123602–7. doi:10.1063/1.3045738.

[36] Cole, J. D., and Aroesty, J., "The Blowhard Problem-Inviscid Flows with Surface Injection," *International Journal of Heat and Mass Transfer*, Vol. 11, No. 7, 1968, pp. 1167–1183. doi:10.1016/0017-9310(68)90033-1.

[37] Kaplan, C., "Effect of Compressibility at High Subsonic Velocities on the Lifting Force Acting on an Elliptic Cylinder," NACA 834, Langley Memorial Aeronautical Laboratory, National Advisory Committee for Aeronautics, Langley Field, VA, May 16 1946.

[38] Tollmien, W., "Grenzlinien adiabatischer Potentialstrmungen," *Zeitschrift fr angewandte Mathematik und Mechanik*, Vol. 21, No. 3, June 1941, pp. 140–152.

[39] Chedevergne, F., Casalis, G., and Féraille, T., "Biglobal Linear Stability Analysis of the Flow Induced by Wall Injection," *Physics of Fluids*, Vol. 18, No. 1, 2006, pp. 014103–14. doi:10.1063/1.2160524.

[40] Chedevergne, F., Casalis, G., and Majdalani, J., "Direct Numerical Simulation and Biglobal Stability Investigations of the Gaseous Motion in Solid Rocket Motors," *Journal of Fluid Mechanics*, Vol. 706, September 2012, pp. 190–218. doi:10.1017/jfm.2012.245.

[41] Beddini, R. A., "Injection-Induced Flows in Porous-Walled Ducts," *AIAA Journal*, Vol. 24, No. 11, 1986, pp. 1766–1773. doi:10.2514/3.9522.

[42] Apte, S., and Yang, V., "Unsteady Flow Evolution in a Porous Chamber with Surface Mass Injection, Part 1: Free Oscillation," *AIAA Journal*, Vol. 39, No. 8, 2001, pp. 1577–1586. doi:10.2514/2.1483.

[43] Apte, S., and Yang, V., "Unsteady Flow Evolution in a Porous Chamber with Surface Mass Injection. Part II: Acoustic Excitation," *AIAA Journal*, Vol. 40, No. 2, 2002, pp. 244–253. doi:10.2514/2.1666.

[44] Wasistho, B., Balachandar, R., and Moser, R. D., "Compressible Wall-Injeciton Flows in Laminar, Transitional, and Turbulent Regimes: Numerical Prediction," *Journal of Spacecraft and Rockets*, Vol. 41, No. 6, November-December 2004, pp. 915–924. doi:10.2514/1.2019.

Appendix A

Series Convergence

The purpose of this Appendix is to analyze the six series that appear in this work. These are

$$S_1 = \sum_{n=2}^{\infty} \frac{\lambda_n^2 \mathcal{I}_{h,n} J_0(\lambda_n r)}{J_1^2(\lambda_n)} \tag{A.1}$$

$$S_2 = \sum_{n=2}^{\infty} \frac{\lambda_n \mathcal{I}_{h,n} J_0(\lambda_n r)}{J_1^2(\lambda_n)} \tag{A.2}$$

$$S_3 = \sum_{n=2}^{\infty} \frac{\mathcal{I}_{h,n} J_0(\lambda_n r)}{J_1^2(\lambda_n)} \tag{A.3}$$

$$S_4 = \sum_{n=2}^{\infty} \frac{\lambda_n^2 \mathcal{I}_{h,n} J_1(\lambda_n r)}{J_1^2(\lambda_n)} \tag{A.4}$$

$$S_5 = \sum_{n=2}^{\infty} \frac{\lambda_n \mathcal{I}_{h,n} J_1(\lambda_n r)}{J_1^2(\lambda_n)} \tag{A.5}$$

$$S_6 = \sum_{n=2}^{\infty} \frac{\mathcal{I}_{h,n} J_1(\lambda_n r)}{J_1^2(\lambda_n)} \tag{A.6}$$

From Sec. 2.1.3, the lowest power of λ_n that appears in the denominator of $\mathcal{I}_{h,n}$ is 3 and the highest to appear in the numerator of the series is 2. It will be hence sufficient to explore in some detail the convergence properties of Eq. (A.1) because the convergence of the remaining series will follow suit. Beginning with Eq. (A.1) and the Poiseuille injection profile whose headwall integral is given by Eq. (2.25), we ignore constant coefficients and write

$$S_1 = \sum_{n=2}^{\infty} \frac{J_0(\lambda_n r)}{\lambda_n J_1(\lambda_n)} \tag{A.7}$$

Now making use of the common asymptotic approximations as $x \to \infty$

$$J_0(x) = \sqrt{\frac{2}{\pi x}} \cos\left(x - \frac{\pi}{4}\right) \tag{A.8}$$

$$J_1(x) = \sqrt{\frac{2}{\pi x}} \cos\left(x - \frac{3\pi}{4}\right) \tag{A.9}$$

$$\lambda_n = \left(\frac{4n-1}{4}\right)\pi \tag{A.10}$$

we can simplify S_1 and write

$$S_1 = \sum_{n=2}^{m} \frac{J_0(\lambda_n r)}{\lambda_n J_1(\lambda_n)} + \frac{4}{\pi\sqrt{r}} \sum_{n=m}^{\infty} \frac{1}{4n-1} \frac{\cos\left[\frac{1}{4}\pi(4nr - r - 1)\right]}{\cos\left[\pi(n-1)\right]} \tag{A.11}$$

where m is some large but finite integer that can be specifically chosen to secure a sufficient level of accuracy between the approximation and the exact solution. Furthermore, using the trigonometric identities,

$$\frac{\cos(a)}{\cos(b)} = \frac{2\cos(a)\cos(b)}{\cos(2b)+1} \tag{A.12}$$

$$\cos(a)\cos(b) = \tfrac{1}{2}\left[\cos(a+b) + \cos(a-b)\right] \tag{A.13}$$

we arrive at

$$S_1 = \sum_{n=2}^{m} \frac{J_0(\lambda_n r)}{\lambda_n J_1(\lambda_n)} + \frac{2}{\pi\sqrt{r}} \sum_{n=m}^{\infty} \frac{1}{4n-1} \left\{ \cos\left[\pi n(r+1) - \tfrac{1}{4}\pi(r-3)\right] \right. \\ \left. + \cos\left[\pi n(r-1) - \tfrac{1}{4}\pi(r-3)\right] \right\} \quad \text{(A.14)}$$

Because the first series is finite, convergence is guaranteed. As for the second series, application of the Dirichlet test can be used to prove that the infinite summation converges. According to Dirichlet, a series given by $\sum_{n=1}^{\infty} a_n b_n$ will converge if a_n will decrease to 0 (i.e., $a_{n+1} \leq a_n$ and $\lim_{n\to\infty} a_n = 0$), and the partial sums of b_n remain bounded (i.e., $|\sum_{n=1}^{k} b_n| \leq M$ for a constant M). By letting $a_n = 1/(4n-1)$, which is clearly decreasing to zero as $n \to \infty$, the first condition is fully satisfied. Furthermore, using the exponential notation for b_n, we can put

$$\begin{aligned} b_n &= \cos\left[\pi n(r+1) - \tfrac{1}{4}\pi(r-3)\right] + \cos\left[\pi n(r-1) - \tfrac{1}{4}\pi(r-3)\right] \\ &= \Re\left\{ e^{-i\frac{\pi}{4}(r-3)} \left[e^{i\pi n(r+1)} + e^{i\pi n(r-1)} \right] \right\} \end{aligned} \quad \text{(A.15)}$$

Using the formula for geometric series, the partial sum can be written as

$$B_k = \sum_{n=1}^{k} b_n = \frac{1}{2} \sec\left(\frac{\pi r}{2}\right) \left\{ \cos\left[\frac{\pi}{4}(4k[r-1] + r + 3)\right] \right. \\ \left. + \cos\left[\frac{\pi}{4}(4k[r+1] + r + 3)\right] + 2\sin\left[\frac{\pi}{4}(r+1)\right] \right\} \quad \text{(A.16)}$$

which remains bounded for all k. At first glance, B_k may be flagged at $r = 1$ where $\sec(\frac{1}{2}\pi)$ appears to be undefined. However, by examining Eq. (A.15), it may be seen that $b_n = 0$ at $r = 1$. This ensures that the second condition of the Dirichlet test is satisfied $\forall r$ and with it, the complete proof that Eq. (A.1) is convergent. The same approach may be used to show the convergence of Eq. (A.4) as well. Nonetheless, it may be instructive to note that at the sidewall Eq. (A.4) becomes dependent on $\sum_{n=2}^{\infty} 1/(4n-1)$, which diverges if unsuppressed. The root of this singularity is discussed in Sec. 2.2.4 along with its successful mitigation through the use of a viscous correction.

For Eqs. (A.2–A.3) and Eqs. (A.5–A.6) convergence may be proven more straightforwardly. For Eq. (A.2), we have

$$S_2 = \sum_{n=2}^{m} \frac{J_0(\lambda_n r)}{\lambda_n^2 J_1(\lambda_n)} + \frac{16}{\pi\sqrt{r}} \sum_{n=m}^{\infty} \frac{1}{(4n-1)^2} \cos\left[\tfrac{1}{4}\pi(4nr - r - 1)\right] \cos\left[\pi(n-1)\right] \quad \text{(A.17)}$$

In the above, the leading coefficient $\sum_{n=1}^{\infty} 1/(4n-1)^2$ may be shown to converge using the comparison test. Additionally, since it can be easily shown that $|(-1)^{n-1} \cos\left[\tfrac{1}{4}\pi(4nr - r - 1)\right]| \leq 1$, the following inequality must hold,

$$\sum_{n=1}^{\infty} \left| \frac{1}{(4n-1)^2} \cos\left[\tfrac{1}{4}\pi(4nr - r - 1)\right] \cos\left[\pi(n-1)\right] \right| \leq \sum_{n=1}^{\infty} \frac{1}{(4n-1)^2} \quad \text{(A.18)}$$

which confirms the absolute convergence of Eq. (A.2). Convergence of Eq. (A.3) and Eqs. (A.5–A.6) can be shown in a similar manner.

Appendix B

Listing of Special Integrals

This appendix contains the special integrals denoted by $\mathcal{I}_n$ in the first order streamfunction. The specification of these integrals as special functions allows the reduction of ψ_1 into a manageable form. The integrals are defined by:

$$\begin{aligned}\mathcal{I}_1 = \int_1^r & Y_1(\lambda_1 r_1) J_1(\lambda_1 r_1) \left\{ J_0(\lambda_1 r_1) J_1(\lambda_1 r_1) \right. \\ & \left. + \lambda_1 r_1 \left[J_0^2(\lambda_1 r_1) + J_1^2(\lambda_1 r_1) \right] \right\} \mathrm{d}r_1\end{aligned} \tag{B.1}$$

$$\mathcal{I}_2 = \int_1^r r_1^3 Y_1(\lambda_1 r_1) J_1^3(\lambda_1 r_1) \; \mathrm{d}r_1 \tag{B.2}$$

$$\mathcal{I}_3 = \int_1^r J_1^2(\lambda_1 r_2) \left\{ J_0(\lambda_1 r_2) J_1(\lambda_1 r_2) + \lambda_1 r_2 \left[J_0^2(\lambda_1 r_2) + J_1^2(\lambda_1 r_2) \right] \right\} \mathrm{d}r_2 \tag{B.3}$$

$$\mathcal{I}_4 = \int_1^r r_2^3 J_1^4(\lambda_1 r_2) \; \mathrm{d}r_2 \tag{B.4}$$

$$\mathcal{I}_5 = \int_1^r Y_1(\lambda_1 r_1) J_0(\lambda_1 r_1) J_1(\lambda_1 r_1) \left[2\lambda_1 r_1 J_0(\lambda_1 r_1) - J_1(\lambda_1 r_1) \right] \mathrm{d}r_1 \tag{B.5}$$

$$\mathcal{I}_6 = \int_1^r r_1 Y_1(\lambda_1 r_1) J_1(\lambda_1 r_1) \; \mathrm{d}r_1 \tag{B.6}$$

$$\mathcal{I}_7 = \int_1^r Y_1(\lambda_1 r_1) R_c(r_1) \; \mathrm{d}r_1 \tag{B.7}$$

$$\mathcal{I}_8 = \int_1^r J_0(\lambda_1 r_2) J_1^2(\lambda_1 r_2) \left[J_1(\lambda_1 r_2) - 2\lambda_1 r_2 J_0(\lambda_1 r_2) \right] \mathrm{d}r_2 \tag{B.8}$$

$$\mathcal{I}_9 = \int_1^r r_2 J_1^2(\lambda_1 r_2) \; \mathrm{d}r_2 \tag{B.9}$$

$$\mathcal{I}_{10} = \int_1^r J_1(\lambda_1 r_2) R_c(r_2)\ \mathrm{d}r_2 \tag{B.10}$$

$$\mathcal{I}_{11} = \int_1^r Y_1(\lambda_1 r_1) R_d(r_1)\ \mathrm{d}r_1 \tag{B.11}$$

$$\mathcal{I}_{12} = \int_1^r J_1(\lambda_1 r_2) R_d(r_2)\ \mathrm{d}r_2 \tag{B.12}$$

Furthermore, in the application of the first order boundary conditions, $\mathcal{I}_7$, $\mathcal{I}_{10}$, $\mathcal{I}_{11}$, and $\mathcal{I}_{12}$ are expanded in such a manner to capture all constants. Doing so leads to the following four expressions:

$$\begin{aligned}\mathcal{I}_7 = k_5 I_{7a}(r) + \frac{3\pi u_h}{2J_1^3(\lambda_1)}\left[-\lambda_1^3 I_{7b}(r) + c_3^2 I_{7c}(r)\right] + k_6 I_{7d}(r) \\ + \frac{3\pi u_h}{2J_1^3(\lambda_1)}\left[\lambda_1^3 I_{7e}(r) - c_3^2 I_{7f}(r)\right]\end{aligned} \tag{B.13}$$

$$\begin{aligned}\mathcal{I}_{10} = k_5 \mathcal{I}_{10a}(r) + \frac{3\pi u_h}{2J_1^3(\lambda_1)}\left[-\lambda_1^3 \mathcal{I}_{10b}(r) + c_3^2 \mathcal{I}_{10c}(r)\right] + k_6 \mathcal{I}_{10d}(r) \\ + \frac{3\pi u_h}{2J_1^3(\lambda_1)}\left[\lambda_1^3 \mathcal{I}_{10e}(r) - c_3^2 \mathcal{I}_{10f}(r)\right]\end{aligned} \tag{B.14}$$

$$\begin{aligned}\mathcal{I}_{11} = k_7 I_{7a}(r) + \frac{\pi}{2J_1^3(\lambda_1)}\left[-\lambda_1^3 I_{7b}(r) + c_3^2 I_{7c}(r)\right] + k_8 I_{7d}(r) \\ + \frac{\pi}{2J_1^3(\lambda_1)}\left[\lambda_1^3 I_{7e}(r) - c_3^2 I_{7f}(r)\right]\end{aligned} \tag{B.15}$$

$$\begin{aligned}\mathcal{I}_{12} = k_7 \mathcal{I}_{10a}(r) + \frac{\pi}{2J_1^3(\lambda_1)}\left[-\lambda_1^3 \mathcal{I}_{10b}(r) + c_3^2 \mathcal{I}_{10c}(r)\right] + k_8 \mathcal{I}_{10d}(r) \\ + \frac{\pi}{2J_1^3(\lambda_1)}\left[\lambda_1^3 \mathcal{I}_{10e}(r) - c_3^2 \mathcal{I}_{10f}(r)\right]\end{aligned} \tag{B.16}$$

where the additional integral functions are defined as

$$I_{7a} = \int_1^r r_1 Y_1(\lambda_1 r_1) J_1(\lambda_1 r_1)\ \mathrm{d}r_1 \tag{B.17}$$

$$I_{7b} = \int_1^r r_1 Y_1(\lambda_1 r_1) J_1(\lambda_1 r_1) \mathcal{I}_1(r_1)\ \mathrm{d}r_1 \tag{B.18}$$

$$I_{7c} = \int_1^r r_1 Y_1(\lambda_1 r_1) J_1(\lambda_1 r_1) \mathcal{I}_2(r_1)\ \mathrm{d}r_1 \tag{B.19}$$

$$I_{7d} = \int_1^r r Y_1^2(\lambda_1 r_1)\ \mathrm{d}r_1 \tag{B.20}$$

$$I_{7e} = \int_1^r r Y_1^2(\lambda_1 r_1) \mathcal{I}_3(r_1)\ \mathrm{d}r_1 \tag{B.21}$$

$$I_{7f} = \int_1^r r Y_1^2(\lambda_1 r_1) \mathcal{I}_4(r_1)\ \mathrm{d}r_1 \tag{B.22}$$

$$\mathcal{I}_{10a} = \int_1^r r_1 J_1^2(\lambda_1 r_1)\ \mathrm{d}r_1 \tag{B.23}$$

$$\mathcal{I}_{10b} = \int_1^r r_1 J_1^2(\lambda_1 r_1) \mathcal{I}_1(r_1)\ \mathrm{d}r_1 \tag{B.24}$$

$$\mathcal{I}_{10c} = \int_1^r r_1 J_1^2(\lambda_1 r_1) \mathcal{I}_2(r_1)\ \mathrm{d}r_1 \tag{B.25}$$

$$\mathcal{I}_{10d} = \int_1^r r_1 Y_1(\lambda_1 r_1) J_1(\lambda_1 r_1)\ \mathrm{d}r_1 \tag{B.26}$$

$$\mathcal{I}_{10e} = \int_1^r r_1 Y_1(\lambda_1 r_1) J_1(\lambda_1 r_1) \mathcal{I}_3(r_1)\ \mathrm{d}r_1 \tag{B.27}$$

$$\mathcal{I}_{10f} = \int_1^r r_1 Y_1(\lambda_1 r_1) J_1(\lambda_1 r_1) \mathcal{I}_4(r_1)\ \mathrm{d}r_1 \tag{B.28}$$